Experimental and numerical study of an aquaculture net cage with floater in waves and current

Trygve Kristiansen[1,*] **and Odd M. Faltinsen**[1]

[1]Centre for Autonomous Marine Operations and Systems (AMOS), Department of Marine Technology, NTNU
Norwegian University of Science and Technology, Trondheim, Norway

[*]e-mail: trygve.kristiansen@ntnu.no

August 28, 2014

Abstract

The mooring loads on an aquaculture net cage in current and waves are investigated by dedicated model tests and numerical simulations. The main purpose is to investigate which physical effects are dominant for mooring loads, and in this respect, to investigate the validity of different rational hydrodynamic load models. Also structural and numerical aspects are investigated. The model tests are performed to provide benchmark data, while the numerical model is used to study the effect and sensitivity of different load models and parameters.

Compared to a realistic aquaculture plant, the total system is simplified to reduce the complexity. The system does, however, include all the four main components of an aquaculture plant: net cage, floater, sinker weights and moorings. The net cage is bottomless, flexible and circular. It is attached to a circular, elastic floater at the top and has 16 sinker weights at the bottom. The system is nearly linearly moored with four crow feet mooring lines.

The loads are measured in the four mooring lines. A systematic variation of current only, wave only as well as combined current and wave conditions is carried out. The numerical simulation results are first benchmarked towards the experimental data. The mean loads in general dominate over the dynamic part of the loads in combined current and waves, and they significantly increase in long and steep waves, relative to current only. Next, a sensitivity study is carried out. A rigid floater significantly alters the loads in the mooring lines compared to a realistic, elastic floater. The theoretical model for the wave matters. The mooring loads are rather insensitive to a majority of the parameters and models, in particular: frequency dependent added mass of the floater and nonlinear restoring loads. It seems not to be necessary to represent the net cage with a very fine numerical mesh.

1 Introduction

Numerical and experimental work for assessing both steady and unsteady behaviour of aquaculture net cages have been presented during the past decades. It is a highly complex, hydroelastic problem with a large number of moving components where all components behave under mutual influence. Therefore, the total system with net cage, floater, mooring lines and bottom weights needs to be considered simultaneously. To facilitate our study, each component is simplified to some extent: the net cage is bottomless (in reality it has a bottom net to close the cage), the floater consists of only one ring (not two attached rings, as is mostly used in reality), the sinker weights consist of 16 single point weights (not bottom weight ring, which is mostly used today), and the moorings are in air and nearly horizontal with linear springs (not submerged and with highly nonlinear properties as in reality). Despite the simplifications, the system is still complex, and a particular challenge is the large differences in length scales; the structure is a combination of large- and small-volume bodies. It is not possible to model the associated hydrodynamic problem directly by first principles (i.e. a Navier-Stokes solver). Therefore, *rational* methods are needed.

Our impression of the research on fish cages is that the hydrodynamic part of the problem is often over-simplified, for instance not considering the shadow effect of a net or properly modelling the

floater. On the other hand, there are many studies using state-of-the art in structural modelling. It has no meaning to consider a sophisticated structural analysis and at the same time have an over-simplified hydrodynamic model. A number of questions are in this respect open as to *what factors are important when modelling fish farms in waves and current*. What effects are most significant for a considered structural response? The main purpose of the present work is to investigate what effects are, and which are not, dominant with respect to mooring loads. The *validity of different rational hydrodynamic load models* is given the main focus. This requires a numerical model which has to be validated. In this work we have further developed the code presented by Kristiansen and Faltinsen (2012a) to also account for regular wave loads. The net cage is here modelled by a truss model. We have compared this with the structural model used by Lader and Fredheim (2006) and Moe et al. (2010) for a net cage in current. The latter study applied the commercial code ABAQUS. They also applied a 3D truss model, but introduced sub-elements such that the trusses were allowed to buckle, and their method was therefore more sophisticated. When we used the same hydrodynamic model as them, i.e. Morison's equation, we got very similar total horizontal and lift force. Furthermore, the net deformation were similar. The agreement with experiments was unsatisfactory for large current velocity. When using our hydrodynamic screen model that accounts for hydrodynamic shadow and Reynolds number effects, the agreement with experiments become satisfactory (Kristiansen and Faltinsen (2012a)). The latter indicates that our structural model is adequate for our studied problem. In order to study net rupture or snap loads one would maybe need an improved structural model. However, that is not our objective in this paper. The research part of the paper is associated with the error analysis. The question is: what effects are most significant for a considered structural response. In our case, the latter is the mooring loads. It could have been contact between a net and chains, or deformation of a weight ring. When it comes to the hydrodynamic problem of the *floater*, we account for the 3D hydroelastic effects. State-of-the-art uses 2D hydrodynamic strip theory, which does not reflect the physics from a hydrodynamic point of view. The latter effect has been investigated in separate studies (Li et al. (2014)). However, in the present study, one question is how does an appropriate hydrodynamic modelling of the floater affect the mooring loads?

Similar fish cage set-ups have been studied experimentally and numerically by Zhao et al. (2007) and Huang et al. (2008). They both demonstrate fair agreement between numerical calculations and experiments for the total mooring line forces. Dong et al. (2010) also considered irregular waves. Xu et al. (2012) studied numerically multiple net cages in waves. Recently, Zhao et al. (2013) developed a numerical strategy to study the flow inside and around flexible fish cages by combining a Navier-Stokes solver with a pressure-drop condition. Two-dimensional studies have also been carried out. A numerical parameter study of a two-dimensional flexible net sheet exposed to waves and current was carried out by Lader and Fredheim (2006). A two-dimensional experimental study was carried out by Bardestani and Faltinsen (2013) with focus on snap loads due to independent motions of the floater and bottom weight when exposed to waves. More references to relevant works are provided in all the mentioned papers.

Common to previous works is that a stiff floater is used (rigid body), and further, there is a rather limitied number of wave/current conditions. In the present paper we present a systematic set of wave/current conditions by varying the wave period, wave steepness and current velocity. The floater model has a realistic bending stiffness (it is highly elastic). Dedicated experimental and numerical work is presented. In particular, we apply the three-dimensional linear potential theory wave load model presented by Li and Faltinsen (2012) for the elastic floater, and the screen type of load model for the viscous force on the net presented by Kristiansen and Faltinsen (2012a). This screen model has not previously been applied to net cages in waves, only steady current cases as documented with good agreement to experimental drag and lift of flexible net cages therein.

Error analysis is rarely addressed in the published marine literature, but is an important aspect of scientific investigations. The work provides in our case results and error analyses that are directly useful for engineering analysis. Furthermore, the paper presents new experimental results.

The present paper is organized as follows. First, a description of the dedicated experiments are

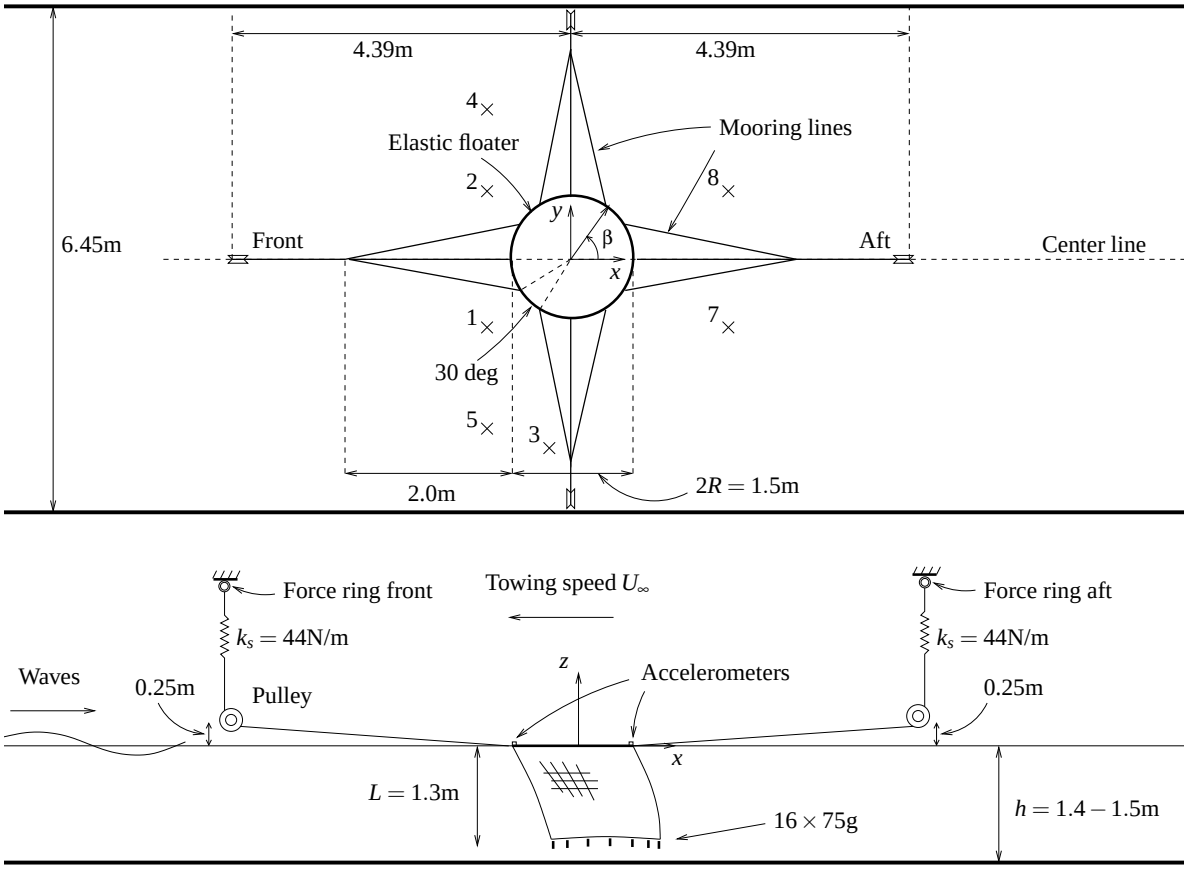

Figure 1: Experimental set-up. Upper: bird's eye view. Lower: side view. Tank dimensions are $L \times B \times h = 40\text{m} \times 6.45\text{m} \times 1.5\text{m}$. A wave maker is located at the far left end of the tank and a parabolic beach at the far right end. The Cartesian coordinate system is located at the origin of the floater in calm conditions. The elastic floater is moored by four moorings; front, aft and two side moorings (no springs in the two latter). The $\times$ markers indicate wave gauges of capacitance type.

described in §2. Next, the numerical model of the net cage, floater, and how the equations of motion for these are coupled is explained in §3. Last, numerical results are compared with the experimentally obtained data in §4, along with a numerical sensitivity study where the effect of different parameters are discussed.

2 Experiments

In order to study the system physically and to obtain validation data, we performed dedicated experiments in the Marine Cybernetics laboratory at NTNU during Fall 2011. The tank length is 26m, the tank width 6.45m and the water depth varies between 1.4 and 1.5m along the tank. The tank is equipped with a hinged flap type wave maker at one end, and a parabolic beach at the other end. It has a carriage for towing models. Current was achieved by towing the model by the carriage towards the waves.

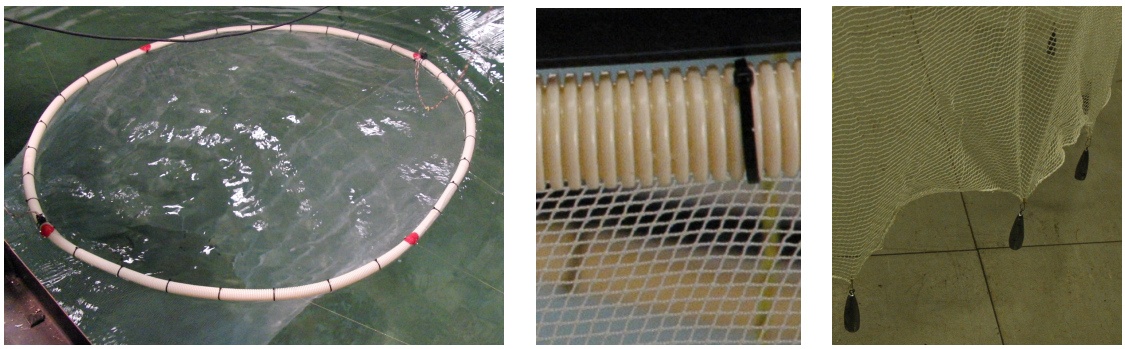

Figure 2: Left: photography from a test with waves and current showing the elastic floater, the net, the mooring lines and the two accelerometers (front and aft). Middle: photography of the floater (tube for electric cables) and the net with one of the 32 strips. Middle: Bottom weights (lead sinkers) and the net.

2.1 Model test set-up

We constructed a model test set-up that involved all the major components of a fish farm, while at the same time keeping the complexity as low as possible. The model test set-up was not intended to represent a specific full scale site. However, assuming a model test scale of 1:25, full scale values are given in Table 1 for reference. Froude scaling with geometric similarity is assumed. This is a requirement for all model tests involving gravity driven water waves. This means that the Reynold's number cannot be properly scaled, but the effects are accounted for in the numerical model, as described later. Note that the presence of sinker weights implies that Froude number is a flow parameter for the pure current case as well.

The test set-up in the experiments consisted of a single net cage attached to a single circular, elastic floater, a bottomless net, 16 sinker weights and four near horizontal moorings with crow feet. See Figure 1. The front and aft mooring were connected to linear springs, pre-tensioned such as to avoid slack mooring lines during the tests. A list of relevant parameters and dimensions of the model are given in Table 1. Photos and snapshots from video illustrating the set-up are presented in Figures 2, 3 and 4. More snapshots for a more complete set of towing velocities in the case of no waves are presented in (Kristiansen 2013).

The instrumentation consisted of force measurement devices in the four moorings, seven wave gauges, two vertical accelerometers and two cameras. The position of the instrumentation is illustrated in Figure 1. Example snapshots from the video are provided in Figure 3. The cameras had a fixed 92 degree wide angle.

2.2 The models

The floater model met the three criteria: (1) a representative bending stiffness EI, (2) a representative cross-sectional diameter $2c$ and (3) a representative specific weight m_f (kg/m). An electric tube of extruded type was used. See the middle photo in Figure 2. The uneven surface represents an uncertainty in the experiments with respect to the environmental loads. The cross-sectional diameter varies between 26mm and 32mm, and the average is approximately 30mm.

Two flexible, bottomless, circular net cages were tested. These were both produced at the SINTEF Fisheries and Aquaculture flume tank in Hirtshals, Denmark. They consisted of nylon threads, constructed in so-called Raschel pattern. The nominal solidity ratios were Sn = 0.26 and 0.32. After testing, we estimated Sn by using an algorithm analysing photos of the nets to be 0.265 and 0.32.

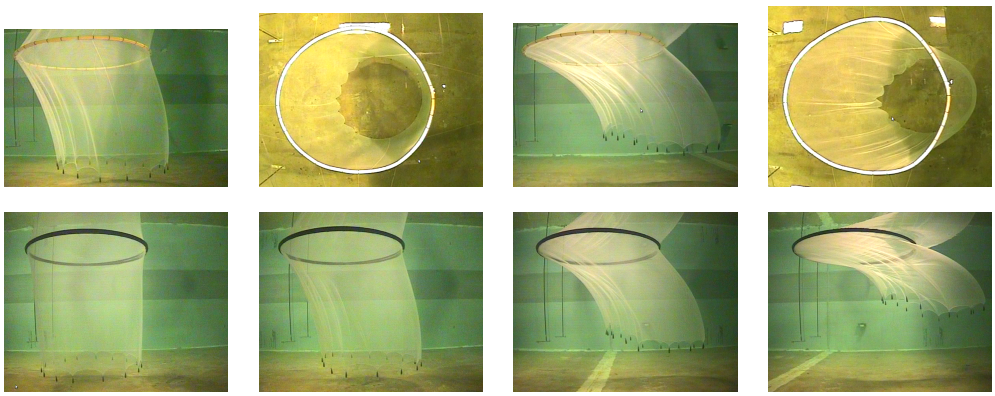

Figure 3: Upper row: snapshots from top camera and underwater camera from tests with the Sn = 0.26 solidity ratio net cage attached to the elastic floater. Two left snapshots: $U_\infty = 0.1$ m/s. Two right snapshots: $U_\infty = 0.2$ m/s. Lower row: from tests with the Sn = 0.32 solidity ratio net cage attached to a stiff floater. From left to right: $U_\infty = 0.04$, 0.1, 0.2 and 0.3 m/s.

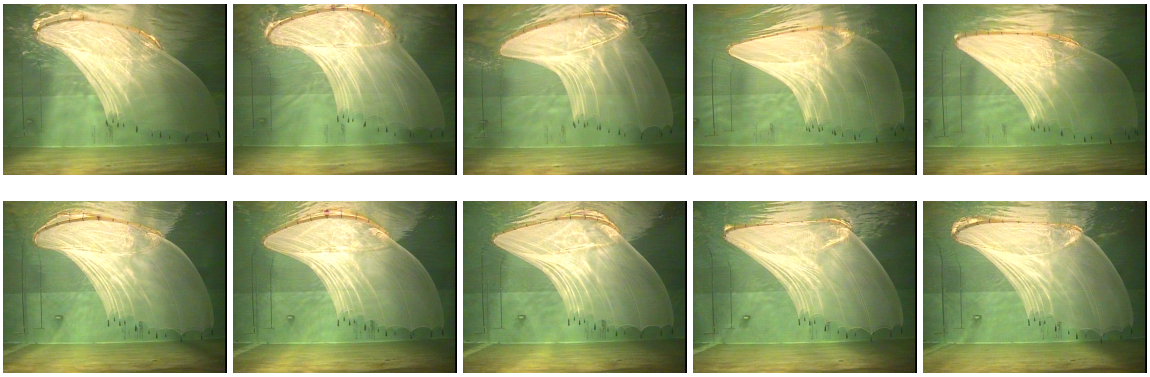

Figure 4: Snapshots from two tests with combined wave and current with $U_\infty = 0.2$ m/s, $H/\lambda = 1/15$. There is approximately $T/5$s between each of the snapshots. Upper row: $T = 1.6$s. Lower row: $T = 1.0$s. The mirror image that appears of the floater clearly indicates that the floater is partly submerged as the wave passes, in particular in the lower row (5sec full scale wave period).

2.3 Test conditions

The test matrix is presented in Table 2. Waves in the period range $T = 0.5 - 1.6$s with a step of 0.05s were tested with three wave height-to-wave length ratios; $H/\lambda = 1/60$, 1/30 and 1/15. H is the wave (trough-to-crest) height and λ the wave length at the water depth of the tank. Wave calibration tests were carried out before the model was tested. An array of seven wave-gauges (see Figure 1) was used to measure the wave elevation in the vicinity of the model position. The wave heights H of the first harmonic component of the measured wave signals were 97 - 99% of the desired, when considering an average of the seven signals.

The main tests were carried out with net cage with solidity ratio of Sn = 0.26 connected to the elastic floater. This model was tested both in waves only, combined waves and current, as well as current only. The model was moored with four moorings with a crow foot arrangement, as illustrated in Figure 1. The net cage with solidity ratio of Sn = 0.32 was connected to a stiff tube. This model was tested in current only.

Table 1: Dimensions in the model tests. The weight of the net cage in water is given in brackets. The bottom weights were made by lead.

Description	Parameter	Model scale	Full scale
Floater diameter	$D = 2R$	1.5m	37.5m
Net cage diameter	$D = 2R$	1.5m	37.5m
Net depth	L	1.3m	32.5m
Cross-sectional diameter of floater	$2c$	30mm	0.75m
Mass per meter of the floater tube	m_f	0.127kg/m	79.4kg/m
Floater bending stiffness	EI	0.136Nm^2	1.33×10^6 Nm^2
Net solidity ratios	Sn	0.26 and 0.32	0.26 and 0.32
Diameter of net twines	d_w	$\simeq 0.6 - 0.8$mm	-
Length of net twines	l_w	6mm	-
Mass of bottom weights in air	M_{bw}	16×75g	16×1172kg
Spring stiffness (front and aft)	k_s	44N/m	27.5kN/m
Mass of the net cage	M_{net}	357g (43g)	5 578kg (672kg)

Table 2: Test matrix showing towing velocity, wave steepness and wave period ranges for each of the two solidity ratio nets.

Solidity ratio Sn	Current U_∞ [m/s]	Wave steepness H/λ		
		1/60	1/30	1/15
0.26	0.0	0.5 - 1.6s	0.5 - 1.6s	0.6 - 1.6s
	0.1	-	0.5 - 1.6s	0.6 - 1.6s
	0.2	-	0.5 - 1.6s	0.6 - 1.6s
	0.04 - 0.30	-	-	-
0.32	0.04 - 0.30	-	-	-

A selection of the tests with combined waves and current as well as current only were repeated at the end of the testing campaign. The repeatability was in general satisfactory; the variations in both mean forces and total forces were less than 3 - 4%. For the force amplitudes, the variations were within 10%.

The carriage velocity was checked with an optical system. It was found to be highly steady, without jerks, and the velocity was calculated to be within 0.2% of the desired value.

2.4 Reduced data

Examples of time-series of the mooring line tension for current only tests are provided in Figure 5, and for combined waves and current in Figure 6. Reduced data by means of mean forces, force amplitudes and total forces in the mooring lines were extracted. These are denoted $\bar{F}$, F_a and F_{tot}, respectively. A near steady part of the time-series was chosen after the initial transient and until the carriage stopped. The measure of the force amplitude was taken as $F_a = \sqrt{2}\,\text{std}(F(t))$, where std means standard deviation, and used throughout this paper. As illustrated in the figures, the loads are different during return of the carriage. This is due to residual current; current generated when towing the model against the waves. This is a well-known issue when towing models. A waiting time of 10min between each run was found necessary and adequate.

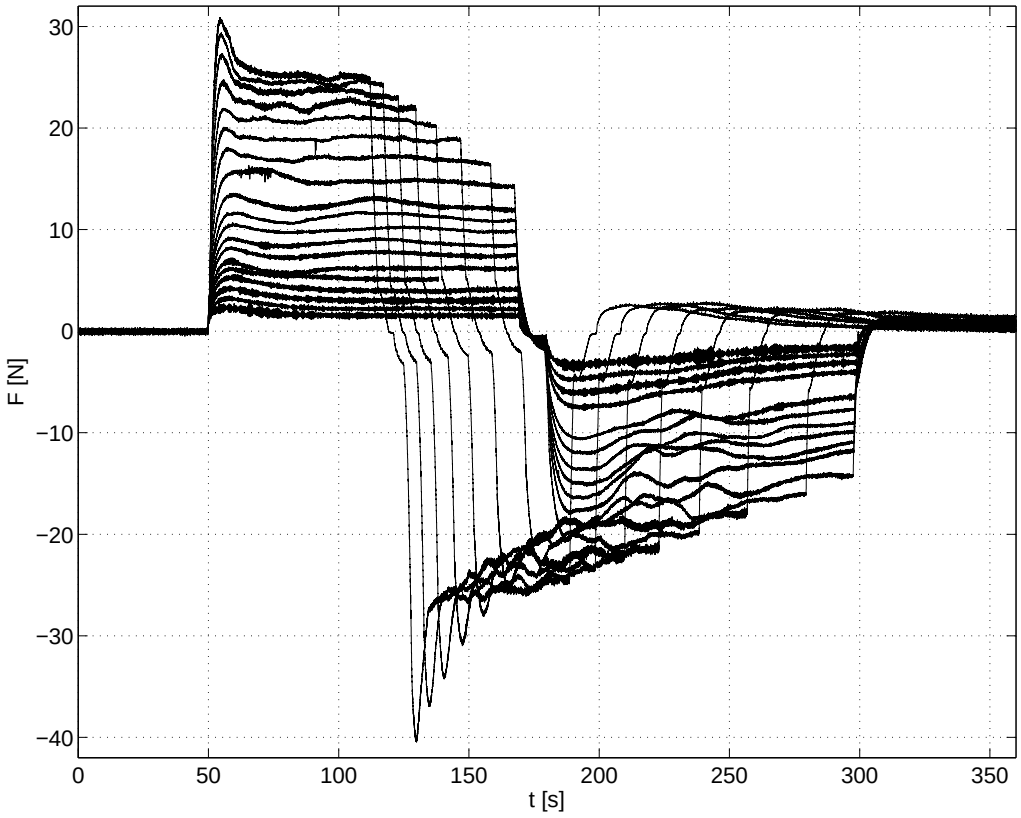

Figure 5: Time-series of the mooring line tension from the 19 towing tests of the model with the net cage with solitidy ratio Sn = 0.32 attached to the stiff (black) floater in current only. The lowest towing velocity was 0.04m/s, and the highest 0.3m/s. Also the return is included for illustration purposes; the forces are higher (in absolute value) upon return. This is due to the residual current caused by the net cage. The mean forces were extracted approximately from just after the initial over-shoot and until the carriage was stopped.

2.5 Observations and comments

2.5.1 Net shape in still water

The net cage shape in still water was not completely vertical; the diameter at the lower end was approximately 10% smaller than at the top. This is the result of the sag in the net cage due to the sinker weights, as seen in other studies also like e.g. Lader and Enerhaug (2005) and Lader et al. (2009). The net cage was connected at 32 evenly distributed connection points along the floater. The angle of the net cage at these connection points was observed to be as large as 30-35 degrees relative to the vertical axis at the connection points. We believe that this had an impact on how the net cage transfers horizontal forces to the floater. The effect of this is investigated in the numerical sensitivity study in §4.3.

2.5.2 Pulley friction in side moorings

Significant friction in the pulleys of the side moorings prevented reliable measurements of the mean forces in these mooring lines. This was discovered after the model tests were done. The mean forces were nearly zero, which is not physical. We therefore do not consider the forces in the side moorings in

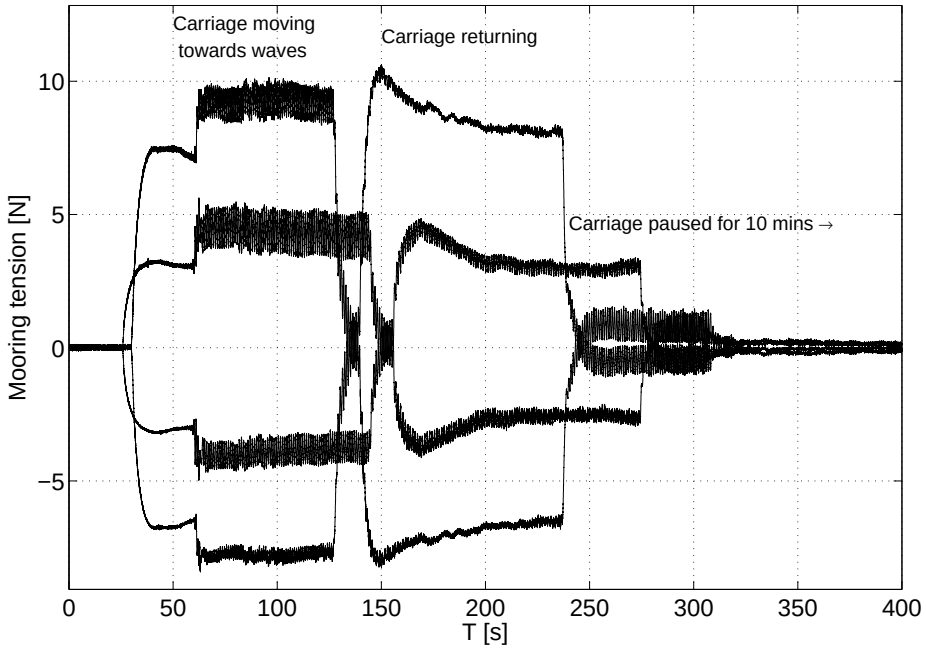

Figure 6: Examples of time-series of tension in the front and aft moorings during an experimental run. $T = 1.1$ s, $H/\lambda = 1/15$ and $U_\infty = 0.1$ and 0.2 m/s. The pre-tension (14 N) is subtracted, hence the negative tension.

the present paper. The friction in the front and aft moorings were, however, small.

2.5.3 Over-topping of the floater

Waves were observed by visual inspection to over-top the floater in several tests. Some of the massive over-topping observed for the steepest waves was most probably in part caused by the second order (Stokes) component of the waves. The observations are summarized in Table 3. *Some* means that a rather thin layer of water runs over the front or aft parts of the floater. *Spilling* means that there is water clearly over-topping front and aft. *Significant* means that most of the floater is over-topped. *Massive* means that the a major part of the floater was at all times submerged, that is, all parts of the floater were at some time-interval not submerged, but fully submerged during most of each wave period. It is expected that appreciable drag was excerted on the front and aft parts of the floater in the cases of significant and massive over-topping.

2.5.4 Seiching

We observed a slight, underlying oscillation with about 21s period in the mooring line forces in some of the tests, which is believed to be due to seiching. Seiching refers to the highest resonance period in a tank. The seiching period of the Marine Cybernetics lab is $T_{seich} = 2L_{\text{tank}}/\sqrt{gh} \simeq 20.9$ s. Seiching will always be triggered to some extent in a closed tank. At the mid-part of the tank, it will be experienced as a slowly varying current. We did not carefully monitor the seiching amplitude through the whole test series, but it was never observed visually to be larger than 0.5cm. The seiching "current" amplitude

Table 3: Observations of over-topping. See Table 4 for the relation between λ/D and wave periods T.

H/λ	U_∞ [m/s]	$\lambda/D < 1$	$1 < \lambda/D < 2$	$\lambda/D > 2$
1/60	0	None	None	None
1/30	0	None	Some	Spilling
	0.1	None	Some	Spilling
	0.2	Some	Some	Spilling
1/15	0	Some	Significant	Significant
	0.1	Some	Significant	Massive
	0.2	Some	Significant	Massive

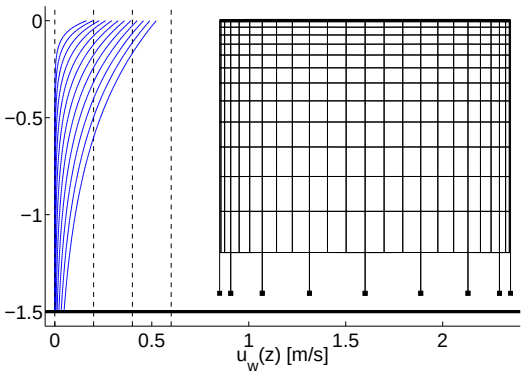

Figure 7: Water particle velocity profiles $u_w(z)$ under a wave as given by linear potential flow theory, for wave periods $T = 0.5, 0.6, .. ,1.6$ s at wave steepness $H/\lambda = 1/15$. For wave steepnesses of 1/30 and 1/60, $u_w(z)$ is one half and one quarter of that shown, respectively. For reference, in the tests with combined waves and current, $U_\infty = 0.1$ and 0.2 m/s. The net cage is here represented by a 48×12 grid, and exponentially varying Δz to better resolve the wave kinematics. The still water line is located at $z = 0$, and the water depth is $h = 1.5$ m.

is then about 0.007 m/s, which is 7% and 3.5% of the two towing velocities of 0.1m/s and 0.2m/s, respectively.

3 Theory and numerical model

In the numerical model, the motion of the net cage, bottom weights, floater and moorings are solved for simultaneously. In brief, first, the hydrodynamic forces acting on the net and floater are calculated. Next, a linear system of equations for the tensions in all the net cage trusses as well as the mooring trusses is solved for. Once the tensions are obtained, the positions of each net cage, mooring and sinker weight node, as well as floater modes are time-stepped according to Newton's second law, using a lumped-mass approach for the net cage nodes.

The next two sections describe in some detail the theoretical model for the net cage and floater, and how they are coupled.

3.1 The net cage

In this section we describe the structural model for the net cage and hydrodynamic force model for the viscous loads on the net cage.

3.1.1 Truss model

The structural model of the net cage in the present paper is the same as that used by Kristiansen and Faltinsen (2012a), and originally presented by Marichal (2003). The main particular of this truss model is that a linear system of equations for the truss tensions is solved each time step. In order to be able to explain how the floater motion is coupled with the net, a brief recapitulation of the truss model is provided. The net is assumed inelastic in this explanation, but (linear) elasticity is straight-forward to include (see Marichal (2003)).

A kinematic constraint on the truss length is imposed; the trusses are required to keep their lengths, i.e.

$$l_k^{n+1} = l_k^n, \tag{1}$$

where l means truss length, superscript n denotes time-step number, subscript k denotes truss number and subscripts i and j refers to nodes. The ends of the truss are given by the nodes $\mathbf{x}_i$ and $\mathbf{x}_j$, such that $l_k^n = |\mathbf{x}_j^n - \mathbf{x}_i^n|$. A first order time-marching scheme is used to evolve the nodes according to Newton's second law,

$$\mathbf{x}_j^{n+1} = \mathbf{x}_j^n + \Delta t\, \mathbf{u}_j^{n+1}, \quad \mathbf{u}_j^{n+1} = \mathbf{u}_j^n + \Delta t\, \mathbf{a}_j^n, \tag{2}$$

where

$$M_j\, \mathbf{a}_j^n = \mathbf{f}_j^n. \tag{3}$$

Δt means time step size, and $\mathbf{u}_j$ and $\mathbf{a}_j$ mean three-dimensional velocity and acceleration vectors of the floater, respectively. M_j is the mass and added mass of the net surrounding the node (lumped mass model). $\mathbf{f}_j^n$ is the force acting on the node, consisting of the tensions in the trusses connected in the node, and the hydrodynamic forces acting on the net surrounding the node. After substituting (2) and (3) into (1) we obtain an equation which is nonlinear in $\mathbf{a}_j^n$, and hence in the tension T. The nonlinear terms are of order $(\Delta t)^3$. Upon neglecting these higher order terms, we obtain

$$\mathbf{s}_k \cdot (\mathbf{a}_j^n - \mathbf{a}_i^n) = -\frac{1}{2l_k}|\mathbf{u}_j^n - \mathbf{u}_i^n|^2 - \frac{1}{\Delta t}\mathbf{s}_k \cdot (\mathbf{u}_j^n - \mathbf{u}_i^n), \tag{4}$$

where $\mathbf{s}_k = (\mathbf{x}_j^n - \mathbf{x}_i^n)/l_k$ is the tangential unit vector of truss number k. On the left hand side we substitute the accelerations with forces according to (3). The *known*, pre-calculated hydrodynamic forces are moved to the right hand side, while the *unknown* tensions are kept on the left hand side. Each truss provides an equation. With N trusses, we obtain a sparse $N \times N$ system of equations, $Ax = b$, for the unknown tensions. After the solution has been obtained, the node positions are evolved according to (2) - (3).

The moorings are treated in the same manner as the net cage; they are modelled as trusses. The linear springs in the experiments are modelled as linearly elastic trusses.

The nodes of the net cage and mooring trusses that are "located at the floater", i.e. the top-most nodes of the net cage, are treated differently than explained above. The accelerations $\mathbf{a}_j^n$ in (4) are there given by the equation of motion for the floater, presented below. Once these accelerations are represented by the floater motion, all parts of the system is solved for simultaneously. This gives a strong coupling between the floater, net cage and moorings.

3.1.2 Hydrodynamic screen force model

The hydrodynamic, viscous force acting on the net cage is modelled by the *screen type* force model presented by Kristiansen and Faltinsen (2012a). The force model was there validated against model

tests of circular, flexible net cages in steady current. The screen type force model provided significant improvements in predicting the drag and lift forces on the net cages relative to those predicted by a Morison type of force model. We next recapitulate the basic parts of the theory, in order to explain how the wave is taken into account in addition to the current.

The net is divided into net panels (flat screens), each with an area A, representing a part of the physical net. Each net panel is assumed to experience viscous normal and tangential forces due a pressure drop proportional to the local, relative flow velocity squared. Alternatively, the normal and tangential forces may be decomposed into drag and lift forces. Thus, the load model predicts both global drag and lift forces on the whole net (not only drag). The instantaneous, relative flow velocity vector $\mathbf{U}_{\text{rel}}$ is taken as

$$\mathbf{U}_{\text{rel}} = \gamma \mathbf{U}_\infty + \mathbf{u}_w - \mathbf{u}_j, \tag{5}$$

where $\mathbf{U}_\infty$ is the ambient current velocity, $\mathbf{u}_w$ the water particle velocity at the position of the node, and $\mathbf{u}_j$ is the velocity of the node. $\gamma = 1$ in the front half of the net, while $\gamma = r$ in the rear half of the net, where r is a flow reduction coefficient that was proposed by Løland (1991). The reduction factor r is used to approximately account for the velocity reduction in the turbulent wake behind a net or screen in steady flow. Note that we assume the *wave* to be undisturbed on the rear part of the net cage; it is only the *steady part* of the flow, i.e. the current, that is reduced by r.

The normal and tangential viscous forces are further assumed to be functions of Sn, Re and θ, where:

- Sn is the solidity ratio of the net (defined as the ratio of the area projected by the screen on a plane parallel to the screen, to the total area contained within the frame of the screen)
- Re is the Reynold's number based on the physical twine diameter d_w of the net, and an estimated maximum velocity at the panel, excluding its motion; $\text{Re} = (\gamma U_\infty + u_{wa})/(1 - Sn)\nu$, where ν is the dynamic viscosity of water and u_{wa} is the velocity amplitude of an undisturbed water particle at the initial position of the net node. The term $1 - Sn$ accounts for the flow speed-up in between the twines. The Reynold's number is calculated prior to the time marching, and u_{wa} is calculated at the node position when the net cage is at rest.
- θ is the angle between the panel normal and the instantaneous, relative flow velocity $\mathbf{U}_{\text{rel}}$. $\theta = 0$ means that the flow is perpendicular to the net panel.

The screen type force model was developed for steady flow. However, due to the high KC numbers with respect to the twine diameter, the flow in waves may be assumed quasi-steady, and the force model is thus considered to be equally applicable to waves.

3.1.3 Incident waves

The wave velocity $\mathbf{u}_w$ in (5) is computed at the instantaneous position of each net node. Two approaches may be chosen in the present code; one approach is classical linear potential flow theory, the other approach is Wheeler stretching. In the former approach, the vertical position at which the wave velocity is evaluated is taken as $\max(z, 0)$, such that the wave velocity is constant above $z = 0$. In the Wheeler stretching approach, the $z-$coordinate is stretched relative to the free surface elevation ζ, according to $z \to ((z+h)/(\zeta+h) - 1)h$, where h is the water depth. Simulation results using both approaches are shown in the sensitivity analysis in §4.3.

Note that there is considerable evidence in the litterature that Wheeler stretching does not realistically represent the kinematics under a wave. This is seen from comparisons with experimentally obtained velocity fields; see for instance (Stansberg, Gudmestad, and Haver 2008) and (Choi 2005). According to their comparisons, linear wave theory predicts the kinematics rather well under both wave

crests and troughs, while Wheeler stretching under-predicts under the wave crest and over-predicts under the wave trough. It is illustrative, however, to include Wheeler stretching in the sensitive study, since it is rather widely used.

3.2 The elastic floater

The floater is assumed to be circular, i.e. a torus, and floating half-submerged when it is at rest. The Earth-fixed coordinate system is shown in Figures 1 and 8. The vertical $z-$axis coincides with the torus axis at rest, is positive upwards, and zero in the mean water line. The current and waves are assumed to be along the $x-$axis, and there is thus no sway motion. The motion of the floater, (x_f, y_f, z_f), is assumed to be a combination of surge as well as perturbations around its originally circular shape in the horizontal plane, as well as purturbations in the vertical direction. We represent both the lateral and vertical perturbations by modal theory (Fourier series), and express them as

$$x_f(\beta,t) = b_1(t) + v(\beta,t)\cos\beta, \quad y_f(\beta,t) = v(\beta,t)\sin\beta, \quad z_f(\beta,t) = \sum_{n=0}^{\infty} a_n(t)\cos n\beta, \tag{6}$$

where

$$v(\beta,t) = \sum_{n=2}^{\infty} b_n(t)\cos n\beta \tag{7}$$

is the lateral (radial) motion. a_0 represents heave, a_1 pitch, a_2 the first vertical elastic mode etc. b_1 represents surge, b_2 the first horizontal mode (ovalization) etc. β is explained in Figure 8.

The radial and vertical structural response is assumed to obey the following beam equations,

$$\begin{aligned} m\frac{\partial^2 v}{\partial t^2} + EI\left(\frac{\partial^4 v}{\partial s^4} + \frac{1}{R^2}\frac{\partial^2 v}{\partial s^2}\right) - \frac{\partial}{\partial s}\left(T_{ax}\frac{\partial v}{\partial s}\right) &= f_r(s,t), \\ m\frac{\partial^2 z_f}{\partial t^2} + EI\frac{\partial^4 z_f}{\partial s^4} - \frac{\partial}{\partial s}\left(T_{ax}\frac{\partial z_f}{\partial s}\right) &= f_z(s,t), \end{aligned} \tag{8}$$

where m [kg/m] is the floater mass per unit length, EI the structural bending stiffness, $\partial/\partial s = R^{-1}\partial/\partial\beta$, and T_{ax} the axial stiffness. f_r and f_z [N/m] are the radial and vertical forces per unit length of the floater, respectively, and include wave excitation force, added mass and damping forces, restoring forces, forces from the net cage and moorings, and drag on the floater;

$$\begin{aligned} f_r &= f_r^{\text{FK}} + f_r^{\text{diffr.}} + f_r^{\text{added mass, damping}} + f_r^{\text{drag}} + f_r^{\text{net cage}} + f_r^{\text{moorings}}, \\ f_z &= f_z^{\text{FK}} + f_z^{\text{diffr.}} + f_z^{\text{added mass, damping}} + f_z^{\text{restoring}} + f_z^{\text{net cage}} + f_z^{\text{moorings}}. \end{aligned} \tag{9}$$

The Froude-Kriloff forces and diffraction forces constitutes the wave excitation forces on the floater. The forces from the net cage and moorings are both transferred to the floater via trusses.

The equation of motion for surge can not be represented by a beam equation, and is therefore treated separately as a rigid body mode,

$$(M + A_{11})\ddot{b}_1 + B_{11}\dot{b}_1 = F_1(t), \tag{10}$$

where $M = 2\pi Rm$ is the total structural mass of the floater, A_{11} and B_{11} are the frequency dependent added mass and damping coefficients in surge, and F_1 is the surge excitation force, consisting of wave excitation, drag on the floater, net cage and mooring forces integrated along the floater.

The expressions (6) - (7) are inserted into (8), and these equations are multiplied by $\cos n\beta$ and integrated from 0 to 2π in order to decouple the modes. The equations of motion for each mode weight

$a_n(t)$ and $b_n(t)$ are then obtained. This is carried out in detail by Li and Faltinsen (2012), where the (linear) generalized wave excitation forces are given analytically. A summary is presented next. The incident deep-water wave potential is given as

$$\varphi_0 = \frac{g\zeta_a}{\omega} e^{i(kx-\omega_e t)} e^{kz}, \tag{11}$$

where i is the imaginary unit, ζ_a is the amplitude of the incoming, regular wave, g the constant of gravity, ω the circular frequency, $\omega_e = \omega + kU_\infty$ the meeting circular frequency as the model is towed against the waves and $k = \omega^2/g$ the wave number. The wave is assumed to propagate along the positive $x-$axis. We assume long wave theory, that is, the waves are much longer than the cross-sectional diameter of the floater, i.e. $\lambda/c \gg 1$, where $\lambda = 2\pi/k$ is the wave length. The equations of motion for the vertical modes are then given by

$$\begin{aligned}\left(m + a_{33}^{(n)}\right)\ddot{a}_n + b_{33}^{(n)}\dot{a}_n + \left(2\rho g c + \frac{EI}{R^4}n^4\right)a_n = \\ \frac{1}{\alpha_n}\left[(1-0.25\pi kc)2\rho g c - \left(\omega^2 a_{33}^{(n)} + i\omega b_{33}^{(n)}\right)\right]\zeta_a J_n(kR)\Re(i^{n+1}e^{-i\omega t}) + f_{z,n}^{gen},\end{aligned} \tag{12}$$

where J_n are Bessel functions of the first kind, $a_{33}^{(n)}$ and $b_{33}^{(n)}$ are added mass and damping coefficients, respectively, and the generalized forces are given by

$$f_{z,n}^{\text{gen}} = \frac{1}{\alpha_n \pi}\int_0^{2\pi} f_z(s,t)\cos n\theta \, \mathrm{d}\theta. \tag{13}$$

Similarly for the radial motion. $\alpha_0 = 2$, and $\alpha_n = 1$ for $n \geq 1$. For lateral modes, $n \geq 2$. In equation (12) the second last term on the left hand side, $2\rho g c a_n$, is the linear restoring force. This may be replaced by a nonlinear restoring force, as discussed below. The first and second terms on the right hand side represent the linear Froude-Kriloff and restoring forces, respectively. It is possible to model nonlinear hydrostatic and Froude-Kriloff forces, as also described below. The last term, the generalized force, consists of the axial stiffness, net cage and mooring forces. The radial generalized force further includes the drag force.

3.2.1 Nonlinear Froude-Kriloff and restoring forces

The Froude-Kriloff force is that acting from the incoming wave as though the wave was undisturbed and the body does not move. We assume long wave-length theory as above, and then have that the nonlinear dynamic Froude-Kriloff and hydrostatic forces are given by

$$f_r^{\text{nonlin. FK}} = \rho A_{\text{sub}} \ddot{r}_w, \tag{14}$$

$$f_z^{\text{nonlin. FK}} = \rho A_{\text{sub}} \ddot{z}_w + \rho g\left(A_{\text{sub}} - 0.5\pi c^2\right), \tag{15}$$

where $\ddot{r}_w$ and $\ddot{z}_w$ are the radial and vertical undisturbed wave particle accelerations at the centre axis of the floater, respectively. A_{sub} is the instantaneously submerged area, which is found based on the difference between the undisturbed incident wave and the local vertical position of the floater.

There are appreciable local diffraction effects which are highly nonlinear in nature due to the locally small-volume character of the structure, see for instance (Kristiansen and Faltinsen 2009). One may discuss whether nonlinear Froude-Kriloff and hydrostatic forces actually represent a more accurate model of the physics, since these scattering effects as well as the flow caused by the torus (floater) velocity are not accounted for.

Note that the *diffraction* force (the second term on the right hand side of (12)) is based on long wave-length theory, and is expressed by the added mass and damping coefficients. Since these coefficients are solutions to the steady-state, linear problem, a nonlinear diffraction force is not obtained.

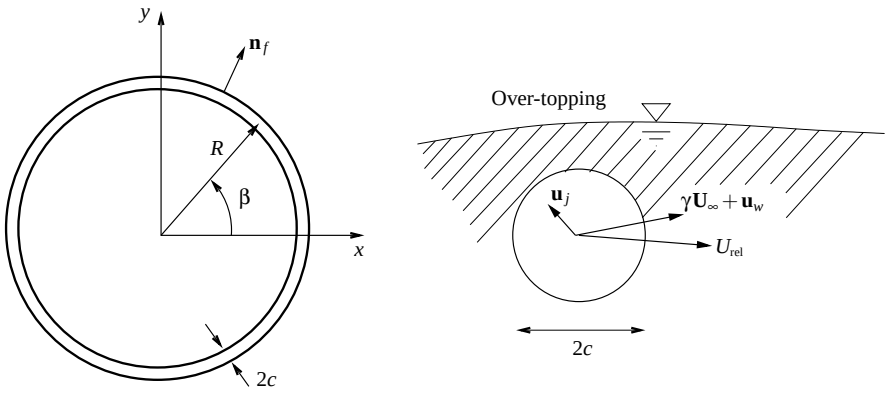

Figure 8: Left: birds-eye view of the floater. Right: cross-section cut of the floater which illustrates over-topping with resulting cross-flow drag in the direction of $\mathbf{n}_f$. The cross-flow velocity is given by $u_c = \mathbf{U}_{\text{rel}} \cdot \mathbf{n}_f$.

3.2.2 Drag on the floater

We apply the drag term in Morison's equation to model the drag force on the floater in the horizontal plane, given by

$$f_r^{\text{drag}}(\beta,t) \quad = \quad 0.5\rho C_D^f \, d_r \, u_r |u_r|, \tag{16}$$

where $d_r(\beta,t) = \zeta - z_f + c$ is the relative submergence, and $u_r(\beta,t)$ is the local, undisturbed, relative cross-flow velocity on the floater; $u_r = \mathbf{U}_{\text{rel}} \cdot \mathbf{n}_f$ (see Figure 8). Here, $\mathbf{n}_f = (\cos\beta, \sin\beta, 0)$ is the two-dimensional unit normal vector of the floater when undisturbed (circular shape).

A drag coefficient $C_D^f = 1.0$ is taken as our nominal guess. We believe that, in reality, the viscous drag on the floater may not be modelled to a high degree of precision using a Morison type of formulation for this problem, as we do here. In case of no over-topping, the free-surface acts as a splitter plate, whereby C_D^f should be lower. For a circular cylinder with splitter plate a representative value for the drag coefficient is 0.6. For high sea-states the floater goes in-and-out of water, and the drag coefficient could be be higher than 1.0. Further, C_D^f depends on the Keulegan-Carpenter number KC as well as the ratio between the wave particle amplitude and current velocity u_{wa}/U_∞ in the case of combined waves and current. The KC number is defined as

$$\text{KC} = \frac{u_{wa} T}{2c}, \tag{17}$$

where u_{wa} is the amplitude of the undisturbed water particle velocity at $z = 0$ as given by linear potential flow theory. Relevant values of these two, and other, parameters for the present study are listed in Table 4.

It is not practical to account for these variations of C_D^f; an attempt would be questionable. We choose to investigate the sensitivity of the floater behaviour with respect to a C_D^f by performing several simulations with different values of C_D^f in order to study the effect of the drag on the mooring loads.

3.2.3 Axial stiffness

The axial tension T_{ax} is treated in a simplified manner. This allows for simplification of calculations, rather than solving the structural problem by a finite element model. The simplified calculation procedure is explained in detail in the Appendix. In summary, T_{ax} is assumed to be piecewise constant along the floater, divided in eight sections defined by the crow-foot mooring arrangement. In calm conditions,

Table 4: Relevant dimensional and non-dimensional parameters describing the test conditions. H is given only for the $1/15$ wave steepness. In the coloumns that presents u_{wa}/U_∞, $U_\infty = 0.1$ m/s.

T [s]		H [m]		λ/D	u_{wa}/U_∞			KC		
1 : 25	1 : 1	1 : 25	1 : 1		1/60	1/30	1/15	1/60	1/30	1/15
0.5	2.5	0.026	0.65	0.26	0.41	0.82	1.63	1.4	2.7	5.4
0.6	3.0	0.037	0.94	0.37	0.49	0.98	1.96	2.0	3.9	7.8
0.7	3.5	0.051	1.27	0.51	0.57	1.14	2.29	2.7	5.3	10.7
0.8	4.0	0.067	1.66	0.67	0.65	1.31	2.61	3.5	7.0	13.9
0.9	4.5	0.084	2.11	0.84	0.74	1.47	2.94	4.4	8.8	17.6
1.0	5.0	0.104	2.60	1.04	0.82	1.63	3.27	5.4	10.9	21.8
1.1	5.5	0.126	3.15	1.26	0.90	1.80	3.59	6.6	13.2	26.4
1.2	6.0	0.150	3.74	1.50	0.98	1.96	3.92	7.8	15.7	31.4
1.3	6.5	0.176	4.39	1.76	1.06	2.12	4.25	9.2	18.4	36.8
1.4	7.0	0.204	5.10	2.04	1.14	2.29	4.57	10.7	21.3	42.7
1.5	7.5	0.234	5.85	2.34	1.23	2.45	4.90	12.3	24.5	49.0
1.6	8.0	0.266	6.66	2.66	1.31	2.61	5.23	13.9	27.9	55.8

the set-up is symmetric, and the values are found in static conditions from the pre-tensions in the moorings. In case of current, the steady current forces from the net is included in the calculation by adding to the pre-tension in the moorings as obtained from simulations. The time-varying line tensions in case of waves are not accounted for in the simplified model.

The axial terms in the beam equations (8) do not decouple, as the other terms do due to orthogonality of the cosines. The axial terms do not decouple because they are integrated piecewise. For the vertical motion, the term representing the axial stiffness in (13) is

$$\frac{1}{\alpha_n \pi} \int_0^{2\pi} \frac{\partial}{\partial s} \left(T_{ax} \frac{\partial v}{\partial s} \right) \cos n\theta \, \mathrm{d}\theta = \sum_{m=0}^{\infty} d_{mn} \, a_m, \tag{18}$$

where

$$d_{mn} = \left(\frac{m^2}{\alpha_n \pi R^2} \sum_{i=1}^{8} T_{ax,i} \int_{\theta_{i-1}}^{\theta_i} \cos m\theta \cos n\theta \, \mathrm{d}\theta \right), \tag{19}$$

and α_n was explained below (13). Similar expressions are obtained for the radial motion.

3.2.4 Equation of motion for the floater

Substituting (12) into the last equation in (6), the generalized vertical equation of motion of the floater becomes

$$\begin{aligned} \ddot{z}_f(\beta,t) = &- \sum_{n=0}^{\infty} \left[b_{33}^{(n)} \dot{a}_n + \left(2\rho g c + \frac{EI}{R^4} n^4 \right) a_n + \sum_{m=0}^{\infty} d_{mn} a_m - \frac{1}{\alpha_n \pi} f_{z,n}^{\mathrm{gen}} \right] \frac{\cos n\beta}{m + a_{33}^{(n)}} \\ &- \sum_{n=0}^{\infty} \left[\frac{1}{\alpha_n} \left[(1 - 0.25\pi kc) 2\rho g c + \left(\omega^2 a_{33}^{(n)} + i\omega b_{33}^{(n)} \right) \right] \zeta_a J_n(kR) \Re(i^{n+1} e^{-i\omega t}) \right] \frac{\cos n\beta}{m + a_{33}^{(n)}}, \end{aligned} \tag{20}$$

and similarly for the horizontal directions. The acceleration $\ddot{z}_f$ in expression (20) is next substituted into $\mathbf{a}_j$ in the kinematic condition (4). The generalized forces, $f_{z,n}^{\mathrm{gen}}$ and $f_{r,n}^{\mathrm{gen}}$, include the truss tensions and remain on the left hand side of (4). The remaining terms in (20) are known, and moved to the right hand side of (4). This serves to include the floater motions in the linear system of equations for the truss tensions, and the floater, net and moorings are thus solved for simultaneously.

The series must in practice be truncated to sums of N_z modes in the vertical direction and N_r modes in the radial direction.

3.2.5 Comments regarding accuracy and computational time

Although the system is sparse, we were not successful in solving by iterative methods; it seems that a high degree of precision in the solution is required, otherwise the solution becomes non-smooth (spikes in the truss tensions), and the simulations then easily become unstable and break down. A direct solution is required. The consequence is a computational time of $O\{N^3\}$, where N is the number of trusses. This leads to rather long computational times if a high spatial resolution is used. Using $N_H \times N_V = 24 \times 8$ grid, however, gives relatively fast computations (2 - 5 minutes running 30 - 80 wave periods on a 2.4GHz laptop). A 48×12 grid results in slow computations (2 - 3 hours). Most numerical simulations presented in the next section is run with a 24×8 grid.

The truncation error of $O\{(\Delta t)^2\}$ in the truss model is in practice very small, since rather small time-steps are needed for stability reasons. From numerical experiments we find that the maximum allowed time-step Δt_{max} is inversely proportional to the smallest truss length. Above this limit, the simulation breaks down immediately (after only a very few time-steps). In the majority of the the present simulations (with 24×8 grid), the minimum truss length is approximately 0.05 m, and the time-step is in the range $2 - 5 \times 10^{-4}$ s. If we run simulations with regular waves with wave period $T = 1$ s, lasting for instance 50 wave periods, this means the number of time-steps will be approximately 100.000 - 250.000, with the corresponding computational times indicated above.

4 Results with numerical sensitivity study

In this last section we present results from the numerical computations and the experiments. The main focus is on the forces in the front and aft mooring lines (see Figure 1). Results from cases with current only are presented in §4.1. Nominal results in the cases with combined current and waves are presented and discussed in §4.2. The sensitivity study is presented in §4.3.

4.1 Current only

Mooring line tensions as obtained from the experiments and numerical simulations from current only tests are presented in Figure 9. The results were also reported in (Kristiansen and Faltinsen 2012b), but included here for completeness. From the right figure, we see that the repeatability in the experiments was rather satisfactory. In particular, the trends are captured.

The different curves are explained in the caption. Note that for the case represented by triangles in the left part of the figure, the presented drag, which is the sum of the forces measured in the front and aft mooring lines, is lower than in the case represented by circles (no spring in the front mooring line), due to the fact that some drag force is absorbed in the side moorings. In the remaining part of the text, it is the set-up *with* spring in the front mooring line (triangles) which has been used.

4.2 Combined waves and current - Nominal results

In this section we present front and aft mooring line tensions, floater motions and excitation forces on the floater, as predicted by the nominal simulations. The mooring line tensions are compared with the experimental data.

Examples of time-series of mooring line tensions in the front and aft moorings are provided in Figure 10 for two selected simulations. The figure shows qualitatively the same as for the experiments in Figure 6; there is, for instance, a clear increase in the mean force when the wave enters. The first one-third of

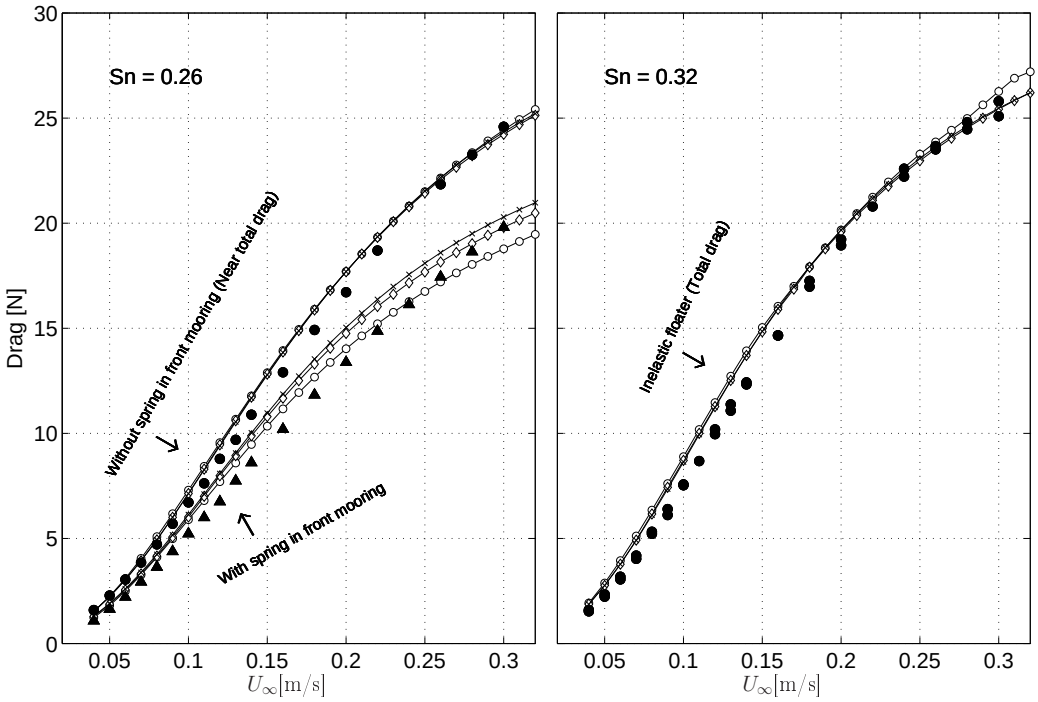

Figure 9: The mean force (drag) decuced from the front and aft mooring lines in current only. Filled symbols: experimental results. Triangular and circular symbols for Sn = 0.26 denote experiments with and without a spring in the front mooring line, respectively (elastic floater and four mooring lines in both cases). The filled symbols for Sn = 0.32 denote experiments with the stiff floater moored only front and aft. Open symbols: present simulations, where circles represent 32×12 mesh, diamonds 48×18 mesh and x-symbols 64×24 mesh.

the simulation was run with current only. x_{off} was taken as the mean position of the floater at the end of this stage. Next, waves were ramped up over 3 periods. The last 10 periods were used for data extraction, as indicated in the figure. The mean force is taken as the mean value within this interval, and the force amplitude taken as $F_a = \sqrt{2}\sigma_F$, where σ_F means standard deviation of the force time-series in the steady time-window. The total force is the sum of the mean force and the force amplitude. This is consistent with the reduced data analysis of the experiments, and gives to our understanding a representative value for the dynamic part of the forces, although the formula is strictly speaking correct only for pure harmonic signals.

Snapshots showing the floater, net cage, moorings and sinker weights are provided in Figure 11. The (linear) wave is included in the top row. In the lower row, the model is illustrated from different angles. The exponential refinement of the mesh towards the upper end of the net cage is illustrated. We mention that for this wave condition, and longer waves, the floater basically follows the waves, although over-topping occurs in the model tests, as discussed earlier (see Table 3). For much shorter waves, the floater is "too stiff" to follow the wave profile.

4.2.1 Mooring line tension

Comparisons are provided in Figures 12 and 13. We chose to present the results with fixed values on the vertical axis, although some details become unclear. This is to illustrate the trends with increasing current velocity. More detailed views of the mean and total forces are provided for the wave only cases

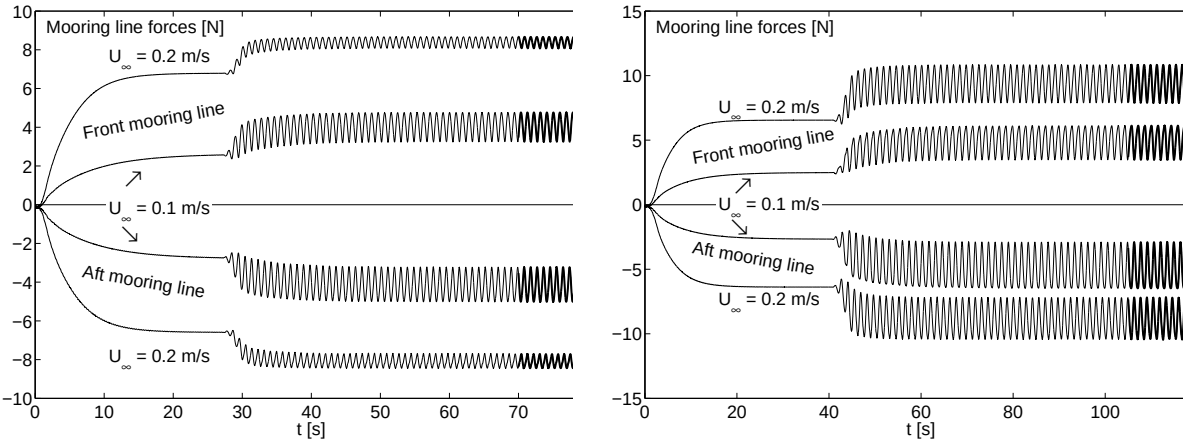

Figure 10: Examples of time-series of the front and aft mooring line tension from numerical simulations with the present code. The pre-tension is subtracted. Two different current velocities: 0.1m/s and 0.2m/s. Left: $T = 1$s and $H/\lambda = 1/15$. Right: $T = 1.5$s and $H/\lambda = 1/15$.

in Figure 14. Note that we present the absolute forces; the aft moorings are actually relaxed (negative) relative to the pre-tension of 14N.

Overall, the agreement is fair. The simulations are in general conservative, except for the force amplitudes in some conditions. Discrepancies up to 25% are observed for some cases ($U_\infty = 0.1$m/s), but it is in general significantly less. Importantly, the *trends* are captured by the simulations. Our main observations are as follows:

- The *trends and magnitudes* of the mooring forces in the front and aft moorings are very similar.
- The *mean* forces in general dominate over the dynamic part in the cases with current.
- The *mean* forces increase nearly linearly with λ/D.
- The force *amplitudes* increase nearly linearly with $\lambda/D \gtrsim 1.5$.
- The force *amplitudes* trends and magnitude are not significantly affected by current.
- The *total* mooring forces are less affected by the wave steepness when the current velocity is high.
- The *total* mooring forces in case of waves only with the highest steepness case, $H/\lambda = 1/15$, are as high as those caused by the medium current of 0.1m/s . Similarly the forces in medium current and longest and steepest wave condition is as high as those in the highest current of 0.2m/s with no waves.
- In the case with 0.1m/s current, the *total mooring force is more than doubled* in the case of the longest, steepest waves, relative to current only. For instance, the experiments predict an increase from approximately 3N to 7N in the front mooring line. This corresponds in full scale to 47kN to 109kN, assuming a model test scale of 1:25 (Froude scaling is assumed).

Considering the wave only case, we see from the three Figures 12 - 14 that the agreement between the simulations and experiments rather good for the lowest steepness wave case, $H/\lambda = 1/60$. This applies to both the mean force, force amplitude and total forces. For the higher steepness cases, the mean forces are significantly over-predicted. We have not succeeded in explaining this, as discussed

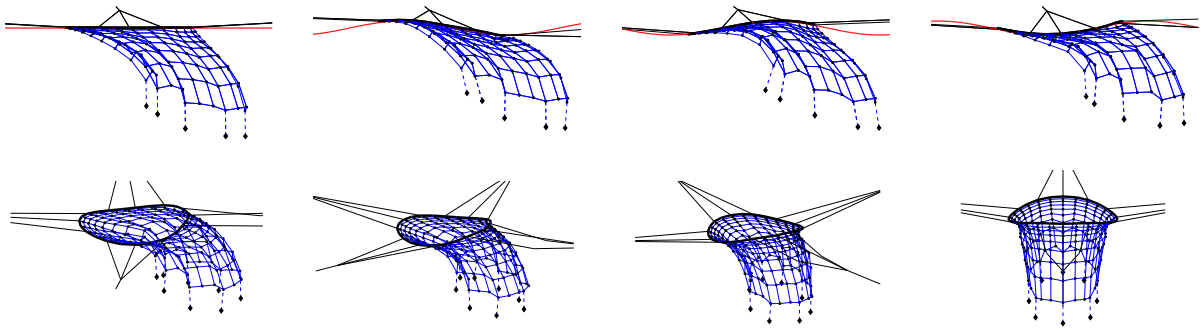

Figure 11: Upper row: Snapshots for different time-steps from present numerical simulations with $N_H \times N_V = 24 \times 8$. Towing velocity $U_\infty = 0.2$m/s, wave period $T = 1.25$s and wave steepness $H/\lambda = 1/15$. The upper left snapshot illustrates the steady shape due to current before the wave is started in the simulation. Lower row: Snapshots for different views for the case presented in the upper right snapshot.

somewhat more in the sensitivity study further below. Concerning the good agreement for the lowest wave steepnesses, we make two comments. First, we find it reassuring that mean forces as low as 0.1N are captured in the experiments, which indicates good quality of the measurements. Secondly, it serves as a validation of the simulation model; the theory and implementation seem to hold for small "linear" waves and motions. This holds even though the net cage does have an appreciable contribution to the forces on the floater, as discussed next.

4.2.2 Excitation forces on the floater

The floater is acted upon directly by wave forces, tension forces from the net cage and tension forces from the mooring lines. The two former terms are considered as excitation forces. In the present work, the forces that act directly on the floater from the waves consist of those predicted by linear potential flow theory as well as quadratic drag, as discussed in §3.2. In the upper part of Figures 15 and 16 we present the excitation forces on the floater for the first two horizontal modes, surge and ovalization. Two terms are included in the figure: one is that predicted by the *linear potential flow theory* (drag not included), the other is that from the *net cage*. The drag forces on the floater are not included, although they are not insignificant for the longest, steepest waves. The same scaling is taken for each sub-figure for direct comparison.

Our main observations are as follows:

- The two contributions are of similar magnitude for the wave conditions $\lambda/D \lesssim 1.3$, while that from the net cage dominates for longer waves.
- This is in particular obvious for the cases with combined waves and current (ref. Figure 16)
- For the longest wave, $\lambda/D \simeq 3.2$, the force in surge from the net cage is about 3-4 and 7-8 times that directly from the waves (as predicted by linear potential flow theory) for $H/\lambda = 1/30$ and $H/\lambda = 1/15$, respectively.

.

In the lower part of Figures 15 and 16 we present the phasing between the two force contributions. The phasing is taken relative to the linear potential theory load, so that for instance 120 deg means that the force from the net cage is 120 behind the other. In order to make the plots more clear to read, we have removed those data points that corresponds to the wave lengths where the excitation forces are at

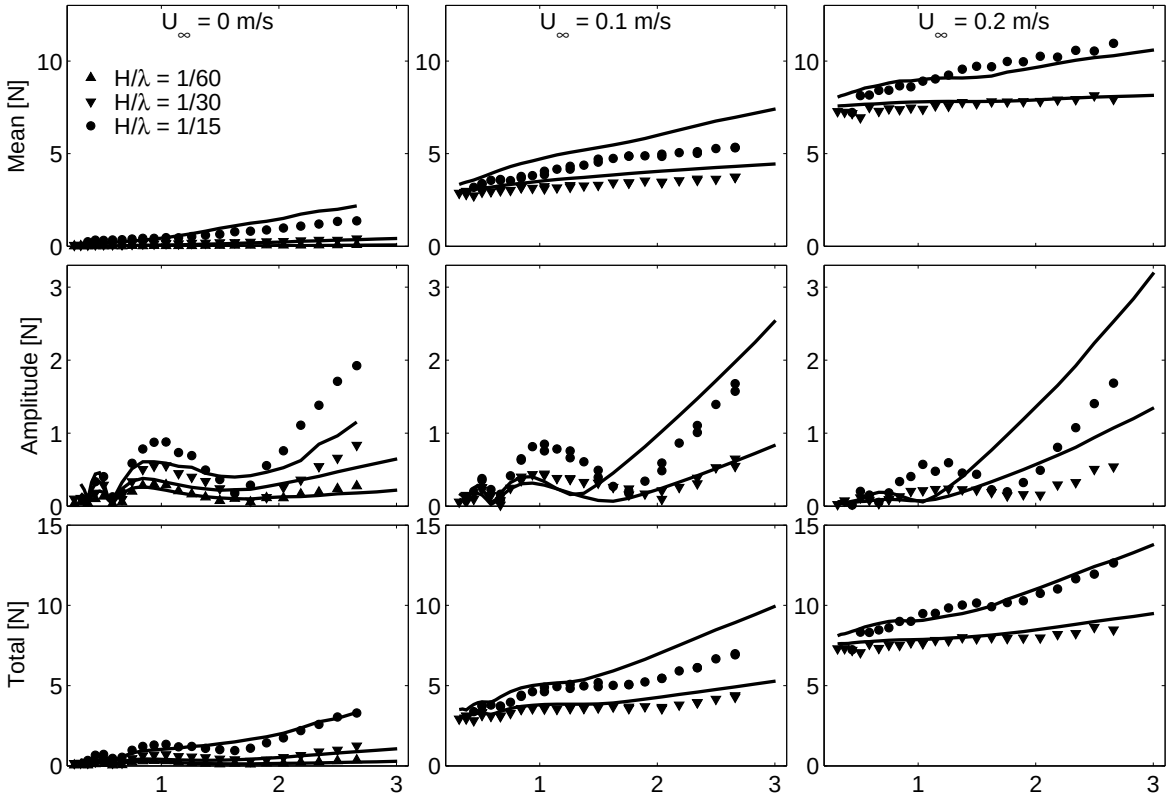

Figure 12: Comparison of mean forces, force amplitudes and total forces in the *front* mooring line from the present model tests (symbols) and present nominal numerical calculations (solid curves).

a minimum in the upper plots, for which the phasing appears to be rather arbitrary. For surge, the phase difference is mainly between 150deg and 210deg. We interpret this such that the net cage opposes the motion of the floater which seems basically to be induced by the waves directly. We mean that, even though the net cage is directly acted upon by the wave itself, it seems to be the floater that "drives" the motion. For sinusoidally varying wave kinematics, acceleration is 90 deg ahead of velocity. Since the potential flow forces acting on the floater are proportional to the wave particle *accelerations*, while the viscous forces acting on the net cage are proportional to the wave particle *velocities*, it is expected that the motion of the floater must be the "driving force", so our observations are reasonable.

4.2.3 Floater motions

The floater motions for the first four modes as predicted by the nominal simulations are provided in Figure 17 for the first four horizontal modes $b_1 - b_4$ and vertical modes $a_1 - a_4$. Equal axes are chosen in order to illustrate the relative contributions to the elastic floater motion. For the horizontal motion, surge and ovalization dominates. The first elastic mode also contributes, but higher modes are nearly negligible with respect to motion of the floater. For the vertical motion, heave and pitch dominates, but higher (elastic) modes also contribute significantly. The latter is in accordance with observations in the experiments by Li et al. (2014).

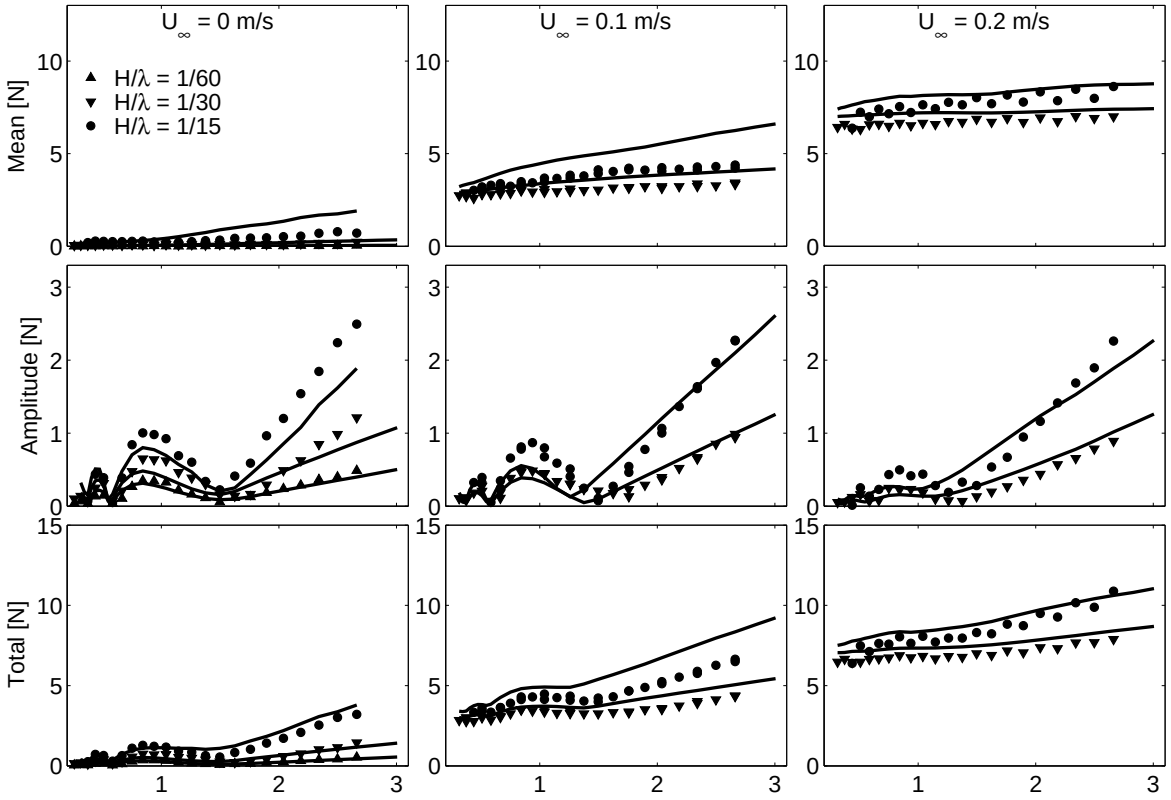

Figure 13: Same as in Figure 12, but for the *aft* mooring line.

4.3 Numerical sensitivity study

The different parameters that are varied are listed in Table 5. In total, there are 32 variations. The parameters are divided into three categories: load modelling, structural modelling and numerical parameters. In order to quantify the significance of the different parameters, and try to identify important ones, we present condensed results in Figures 18 and 19. In Figure 18, each bar represents the percentagewise difference of the total mooring line tension with respect to the nominal value, averaged over all the tested wave periods. As seen from the figures, each parameter has different impact on the mooring line tension for each of the seven different cases (each case is one combination of current speed and wave steepness). This provides rather detailed information about the effect of each parameter on each of the seven cases.

In Figure 19 each bar represents the mean of the absolute value of the condensed data presented in Figure 18. We have chosen to present in detail the effect of those parameters that impose more than 5% difference. These are marked by an x in Table 5. The detailed results are presented in Figures 20 - 23. One general observation is that the mean forces are more sensitive to parameter variations than the force amplitudes. More detailed discussions are presented in the following.

4.3.1 Load modelling

In Figure 20 load parameters are varied. From Figure 19, Wheeler stretching seems to have the largest effect of the load parameters. As seen from the more detailed Figure 18 and Figure 20, it has the largest effect on wave only cases. It has less effect on the cases with combined waves and current. Note that, as mentioned in §3.1.3, Wheeler stretching is not a physically correct wave model, and can not be

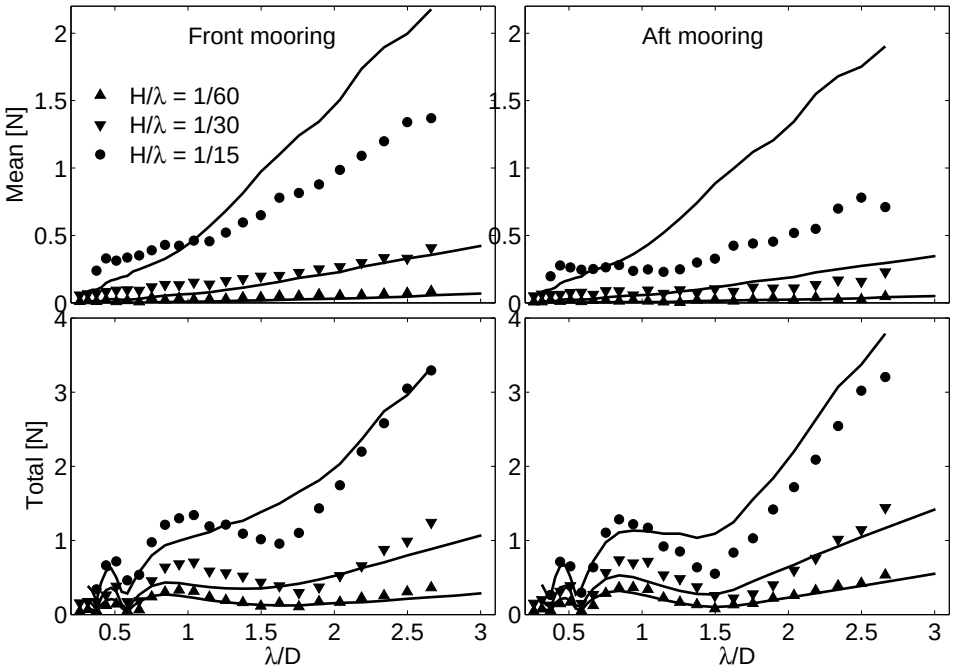

Figure 14: Comparison of mean and total forces in the front and aft mooring lines for zero current cases only (zoom of upper left and lower left sub-figures of Figures 12 and 13).

recommended. The presented results indicate merely that modelling of the incoming wave kinematics, i.e. the velocity for the quadratic drag on the net, is of importance. Nonlinear Froude Kriloff and restoring forces also has an effect, but our results do not indicate an improvement over the nominal results. The wake reduction factor r does have influence in the cases with combined current and waves. This is consistent with the sensitivity study presented by Kristiansen and Faltinsen (2012a).

The mooring loads do not seem to be sensitive to the offset, x_{off} (see also the discussion in relation to Figures 15 and 16). It thus seem that the total system is not very sensitive to phasing between the viscous forces on the net cage, and the wave forces on the floater. In general, the effect of drag on the floater is quite moderate. Modelling the three-dimensional, frequency-dependent added mass does not seem to be important for the mooring loads.

4.3.2 Structural modelling

In Figure 21 structural parameters are varied. Varying the cross-sectional diameter of the floater, $2c$, has a direct effect on the wave excitation forces. Note that, in these simulations, also the bottom weights are adjusted to account for the change in buoyancy in order to keep the floater semi submerged. The effect that we see is probably significantly affected by this. A larger bottom weight will result in higher drag in current, due to less deformation of the net cage. We see that the effect is rather modest in the wave only cases. Increasing the bending stiffness of the floater, EI, with a factor of 25, has a significant effect on the mean and total forces in the cases with combined current and waves. The reason for choosing the factor 25 was inspired by the fact that if one geometrically scale the model, using the same material as in full scale, the model will be too stiff by a factor equal to the model scale, which in our case is taken to be 1:25. In the cases with the highest current, $U_\infty = 0.2$m/s, the mean and total forces in both the front and aft mooring lines are approximately halved. The reason is not that the loads are reduced, but rather that the side moorings absorb the remaining loads. This will not be equally pronounced in a more realistic

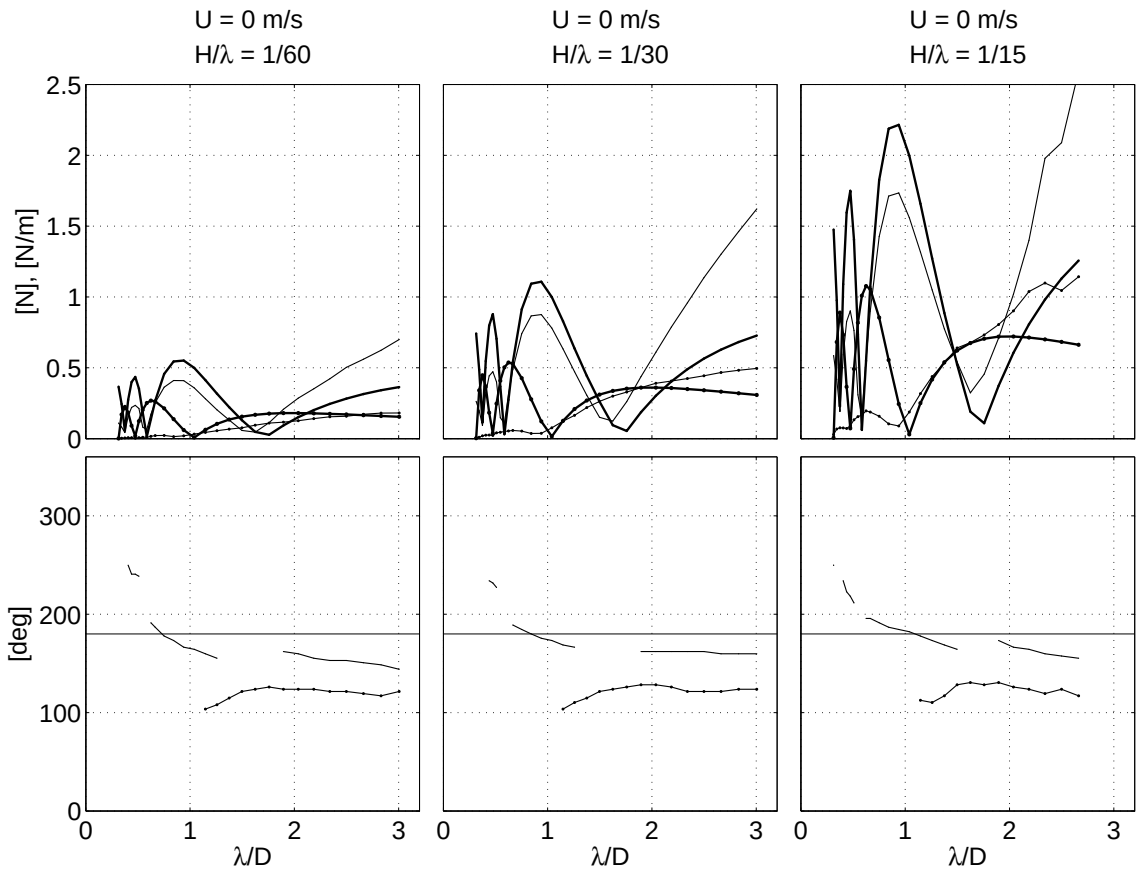

Figure 15: Radial excitation forces (upper) and relative phasing (lower) on the floater as calculated by the present code. Thick curves: the analytically expressed wave excitation load. Thin curves: Load from the net cage. Solid curves: surge [N]. Curves with dots: second mode (ovalization) [N/m]. The phasing is taken relative to the force from the waves. The same scaling is taken for each sub-figure for comparison purposes.

setting where there is significantly less pre-tension in the moorings. However, this still demonstrates that modelling the stiffness of the floater correctly in the model tests is of importance. The axial stiffness is in the present study modelled by the approximate method described in §3.2.3, with piecewise constant values as listed in Table 6. In the simulations represented by the purple curves in Figure 21, T_{ax} is taken to be uniformly equal to 10N. Thus, the floater should be slightly more stiff, and more forces should be absorbed in the side moorings. This is what we observe.

In Figure 22 further structural parameters are varied. Changing the diameter of the net and floater, D, by 10% changes the total loads by a similar, but slightly smaller amount. According to Figure 19, the change is about 6 - 7%. This less-than-linear dependency on D is consistent with the sensitivity presented by Kristiansen and Faltinsen (2012a). Modelling the net cage (unrealistically) too elastic has a sinificant effect on the mooring loads, in particular in the aft mooring line. The purpose was to try to model "geometric elasticity" in the net cage. The shape of the net cage, after some initial simulation, is shown in the upper right corner of Figure 24. We conclude that this way of modelling the geometric elasticity is obviously wrong. The "nominal" and "initial" shapes are also shown in the figure. Using a prescribed "initial" shape as described earlier does have some effect, most so on the force amplitudes in

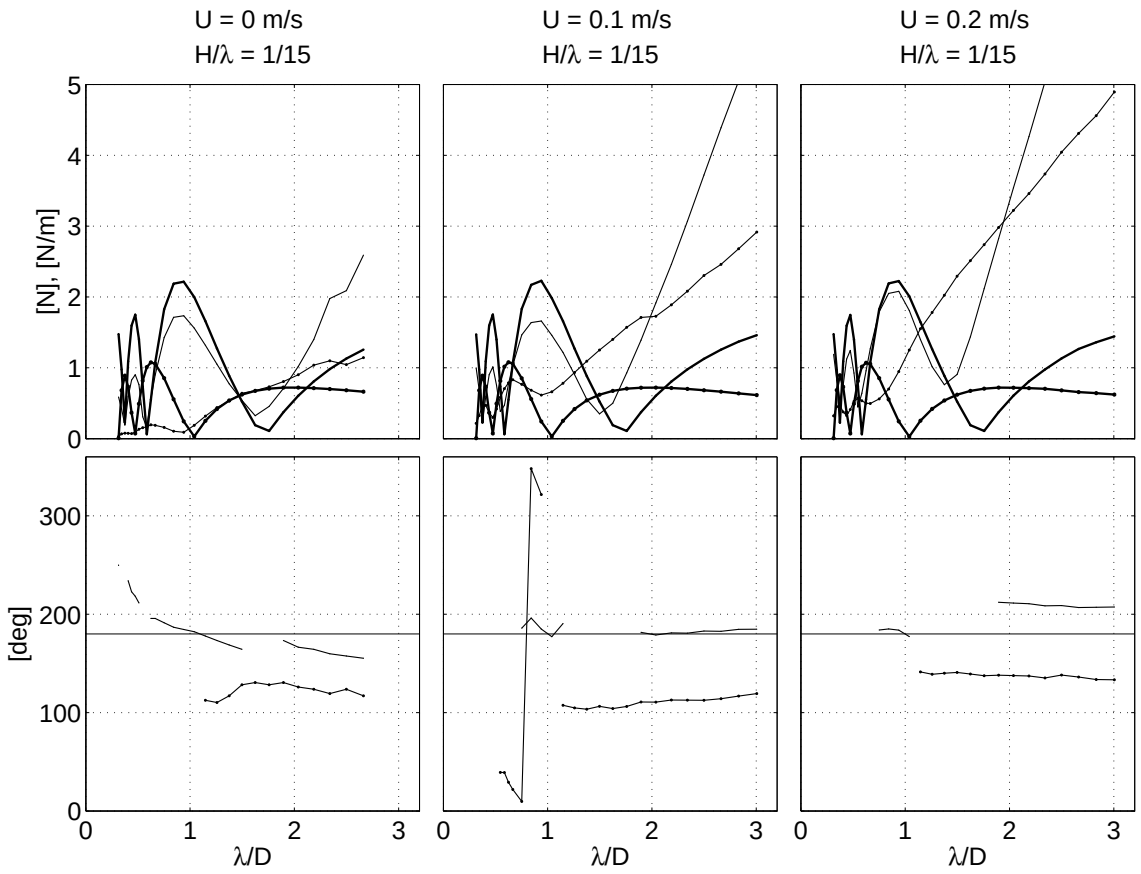

Figure 16: Same as in Figure 15, but for the vertical direction. The force from the net cage reaches 5.6N in the upper middle plot, and 8.4N in the upper right plot.

the case of waves only. However, it does not seem to provide improvement over the nominal, straight-walled net cage shape. In the cases with combined waves and current, the initial shape seems to have limited effect.

The mooring loads do not seem to be sensitive to net depth, L, solidity ratio Sn, pre-tension T_p or mooring line stiffness k_s, and neither elasticity of the net twines as long as this is in a sensible range ($EI = 5 \times 10^8 \mathrm{Nm}^2$ is representative for nylon).

4.3.3 Numerical modelling

In Figure 23 numerical parameters are varied. It is clear that modelling the floater as a rigid body has a pronounced effect on the mooring forces. The effect is similar to using 25 times too stiff floater, as described above. The same comments thus apply to the present discussion. Using too few modes, in this case only 4 in both the lateral and vertical directions, has similar, but less pronounced effects. From the remaining parameter variations with higher density meshes (variation no. 31 and 32), we find that 8 modes are sufficient for convergence in the present set-up. As we see from Figures 18 and 19, the variations from nominal values are in the range 3 - 4%. This is also reassuring with respect to the validity of the present sensitivity study which is carried out with a rather coarse mesh. The meshes are

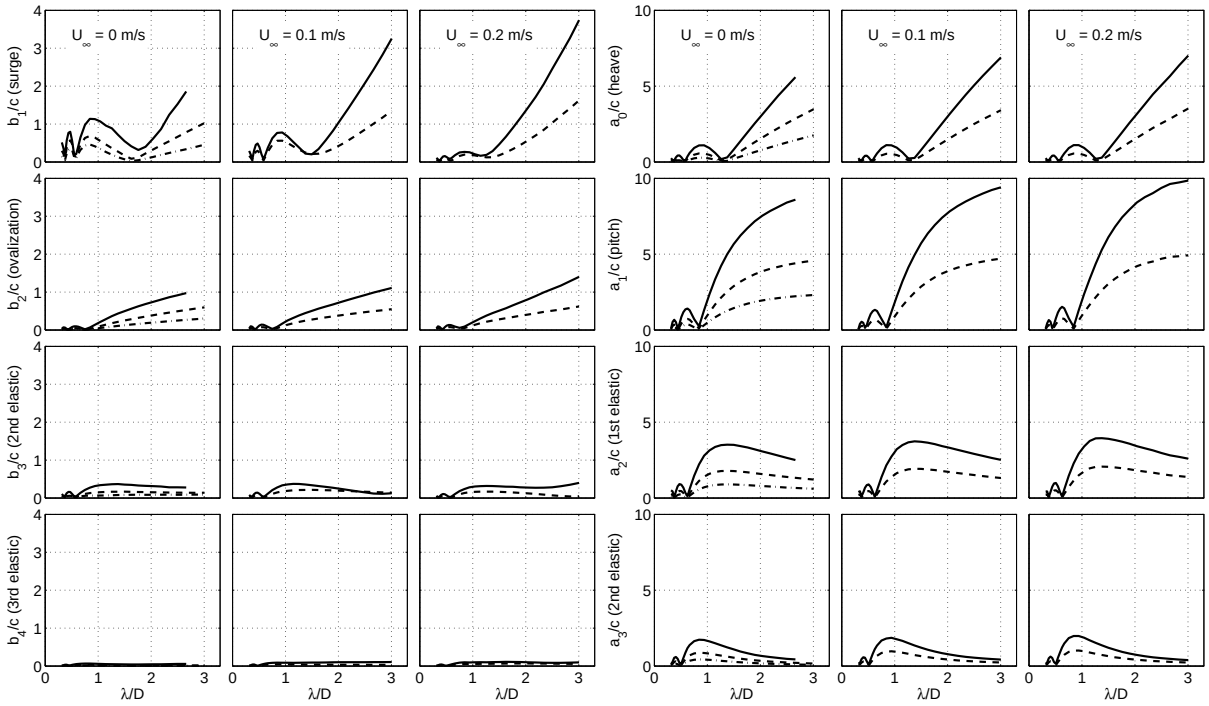

Figure 17: Four lowest mode ampliudes as obtained by nominal simulations. Left: horizontal modes. Right: vertical modes. Dash-dot curves: $H/\lambda = 1/60$. Dashed curves: $H/\lambda = 1/30$. Solid curves: $H/\lambda = 1/15$.

illustrated in the lower part of Figure 24.

We would like to emphasize that parameters that are not important to mooring loads, may still be important for instance for local motion. The present sensitivity study has been concerned with mooring loads only. Examples are drag on the floater and nonlinearities associated with over-topping. These local effects may, for instance, be important for snap loads, as investigated e.g. by Bardestani and Faltinsen (2013).

5 Conclusions

We presented a study on a circular, flexible, bottomless net cage with sinker weights attached to a circular, elastic floater exposed to waves and current. The floater was nearly horizontally moored with four mooring lines with crow feet. Dedicated experiments were carried out, and a numerical model implemented. A representative range of wave periods, wave steepness and current velocities were tested. Tests with current only, combined current and waves as well as waves only were performed. Mooring loads were compared. Satisfactory agreement between simulations and experiments was demonstrated.

A number of questions are still open as to *what factors are important when modelling fish farms in waves and current*. It is not feasible to solve this hydro-elastic problem from first principles. In particular for the hydrodynamic loads, rational methods are needed. The main purpose of the present work was to identify *what are the dominating factors*, and in this respect, investigate the *validity* of different rational hydrodynamic load models. Structural aspects and numerical aspects were also investigated.

In order to do so, a numerical sensitivity study was presented, where in total 32 variations of rational

Table 5: Parameters that are varied in the sensitivity study. Quantities with subscript 0 means nominal values, as given in Table 1. Nominal net cage mesh: $N_H \times N_V = 24 \times 8$. Nominal vertical mesh distribution is exponential (see e.g. Figure 11). Nominal number of modes are $N_h = N_v = 8$. Right column indicates which parameters that are investigated in detail in connection with Figures 20 - 23.

		No.		Explanation	>5%
Loads		1	-	Wheeler stretching (§3.1.3)	x
		2	$x_{\text{off}} = 0\text{m}$	Offset wave (§3.1.3)	
		3	$x_{\text{off}} = 1.5\text{m}$	"	
		4	$C_D^f = 0$	Floater drag (§3.2.2)	
		5	-	Nonlinear FK+rest. (§3.2.1)	x
		6	$r = 0$	Reduction factor (§3.1.2)	x
		7	$a_{33}^n(0)$	Floater added mass (§3.2)	
Structural	Floater	8	$2c = 0.028\text{m}$	Cross-sectional diameter	x
		9	$2c = 0.032\text{m}$	"	x
		10	$EI = 0.5EI_0$	Bending stiffness floater	
		11	$EI = 2EI_0$	"	
		12	$EI = 25EI_0$	"	x
		13	$T_{ax} = 0\text{N/m}$	Axial stiffness (§3.2.3)	
		14	$T_{ax} = 10\text{N/m}$	"	
	Net	15	$L = 1.17\text{m}$	Net depth	
		16	$L = 1.43\text{m}$	"	
		17	$D = 1.35\text{m}$	Net and floater diameter	x
		18	$D = 1.65\text{m}$	"	x
		19	$E_{\text{net}} = 5 \times 10^8 \text{Nm}^2$	$E-$module of net twines	
		20	$E_{\text{net}} = 1 \times 10^6 \text{Nm}^2$	"	x
		21	$\text{Sn} = 0.9\text{Sn}_0$	Solidity ratio of the net cage	
		22	$\text{Sn} = 1.1\text{Sn}_0$	"	
		23	-	Initial net shape (§2.5.1)	x
	Moorings	24	$T_p = 10\text{N}$	Pre-tension moorings	
		25	$T_p = 18\text{N}$	"	
		26	$k_s = 40\text{N/m}$	Spring stiffness moorings	
		27	$k_s = 48\text{N/m}$	"	
Numerical		28	-	Vertical meshing uniform	
		29	$N_h = 1, N_v = 2$	Rigid body motions	x
		30	$N_h = 4, N_v = 4$	Less modes	x
		31	$N_H = 32$	Mesh resolution	
		32	$N_H = 48, N_V = 12$	"	

models and parameters were made. Load models and structural and numerical parameters were varied. The influence of these was discussed. The study suggested that the mooring loads are not particularly sensitive to any of the variations. Two examples where the modelling was not reasonable were (1) modelling the elastic floater as rigid, and (2) applying an unrealistically low stiffness of the nylon in the net cage. In these cases the mooring loads differed by up to 30% from the nominal loads. The theoretical model for the wave mattered. For all other parameters, the variations in the mooring loads were within 6 - 7% with respect to the nominal loads. The mooring loads were not sensitive to the wave load model for the elastic floater. It was not necessary to represent the net cage with a very fine numerical mesh; a rather coarse mesh was found adequate. The mean forces in general dominated over the force amplitudes in

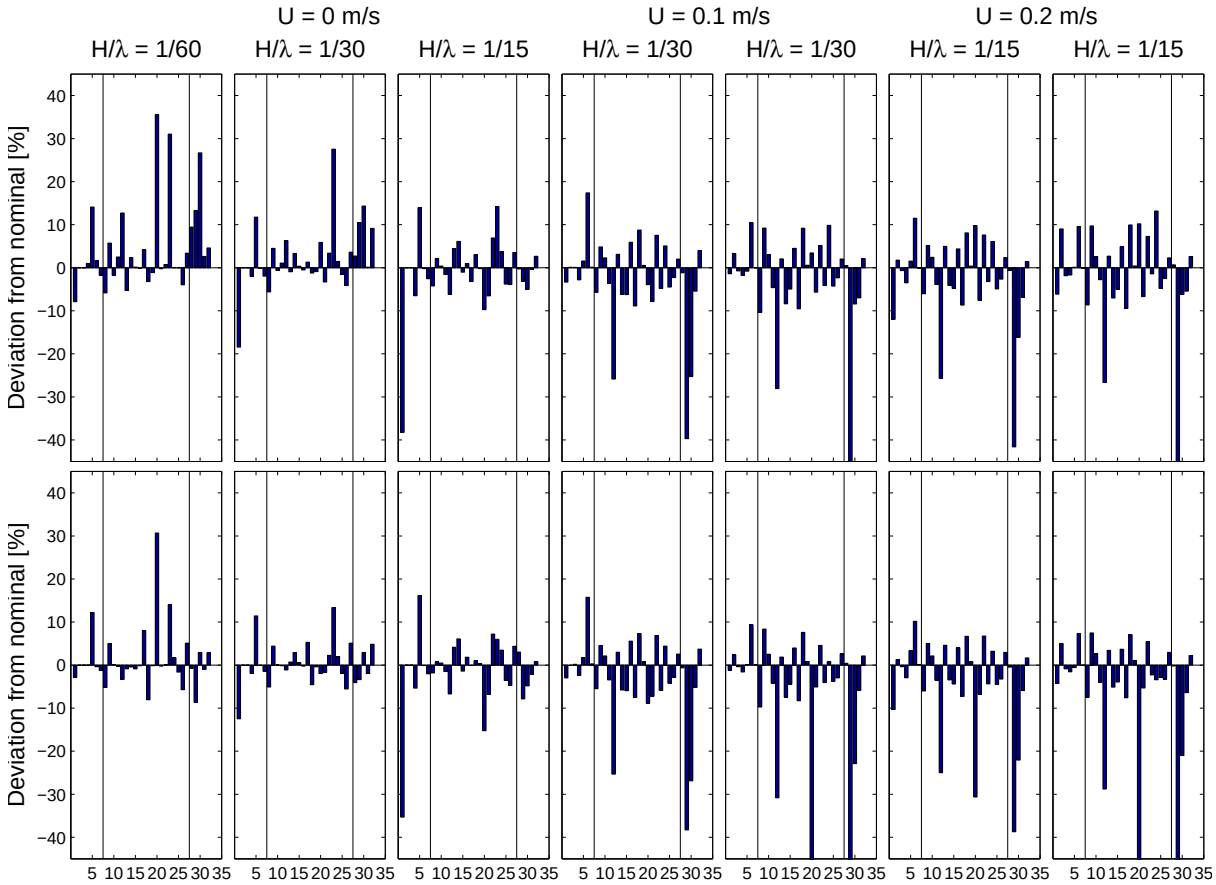

Figure 18: Condensed data. Each bar represents the percentagewise difference of the total mooring line tension with respect to the nominal value, averaged over all the tested wave periods. The numbers on the horizontal axis refer to variation number as given in Table 5. Upper: front mooring line. Lower: aft mooring line.

the cases with combined current and waves. The relative importance, and phasing between inertia and viscous loads were discussed.

For future work one should investigate a more complete fish farm set-up, including bottom net, sinker weight ring, possibly chains connecting the floater and sinker weight ring, two concentric floater rings, and more realistic moorings with less pre-tension and nonlinear properties. Sensitivity studies should be carried out, with an extended range of physical parameter variations. Note that, although we did not identify a set of parameters for which the mooring loads are sensitive, the sum of the uncertainties may be considerable. We believe that it is necessary to perform sensitivity studies for other set-ups in order to try to identify sensitive parameters.

Acknowledgements

We acknowledge that all of the work described in this paper, including both the experiments and numerical work, has been carried out within Centre for Autonomous Marine Operations and Systems (AMOS) at NTNU. We would further like to thank Tore Søreide for deriving the simplified calculations of axial stiffness in the floater, as described in the Appendix.

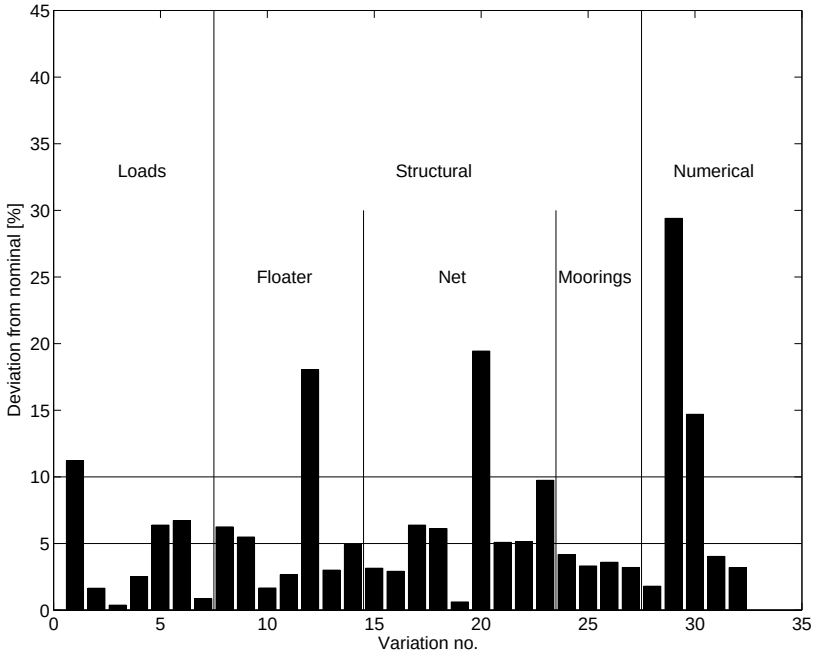

Figure 19: The mean of the absolute value of the condensed data presented in Figure 18.

References

Bardestani, M. and O. M. Faltinsen (2013). A two-dimensional approximation of a floating fish farm in waves and current with the effect of snap loads. In *32nd Int. Conf. Ocean, Offshore and Arctic Engng. (OMAE2013-10487)*.

Choi, H.-J. (2005). *Kinematics measurements of regular, irregular, and rogue waves by PIV/LDV*. Ph. D. thesis, Texas A & M.

Dong, G.-H., T.-J. Xu, Y.-P. Zhao, Y.-C. Li, and F.-K. Gui (2010). Numerical simulation of hydrodynamic behavior of gravity cage in irregular waves. *Aquacultural Engng. 42*, 90–101.

Huang, C.-C., H.-J. Tang, and J.-Y. Liu (2008). Effects of waves and currents on gravity-type cages in the open sea. *Aquacultural Engng. 38*, 105–116.

Kristiansen, D. and O. M. Faltinsen (2009). Non-linear wave-induced motions of cylindrical-shaped floaters of fish farms. *J. Engng. Maritime Env. 223*, 361–375.

Kristiansen, T. (2013). A parameter study on current forces on circular aquaculture net cages. In *32nd International Conference on Offshore Mechanics and Arctic Engineering, Nantes*.

Kristiansen, T. and O. M. Faltinsen (2012a). Modelling of current loads on aquaculture net cages. *J. Fluids and Structures 34*, 218–235.

Kristiansen, T. and O. M. Faltinsen (2012b). Mooring loads of a circular net cage with an elastic floater in waves and current. In *6th Int. Conf. on Hydroelasticity in Marine Technology*.

Lader, P. and B. Enerhaug (2005). Experimental investigation of forces and geometry of a net cage in uniform flow. *IEEE J. Oceanic Eng. 30*, 79–84.

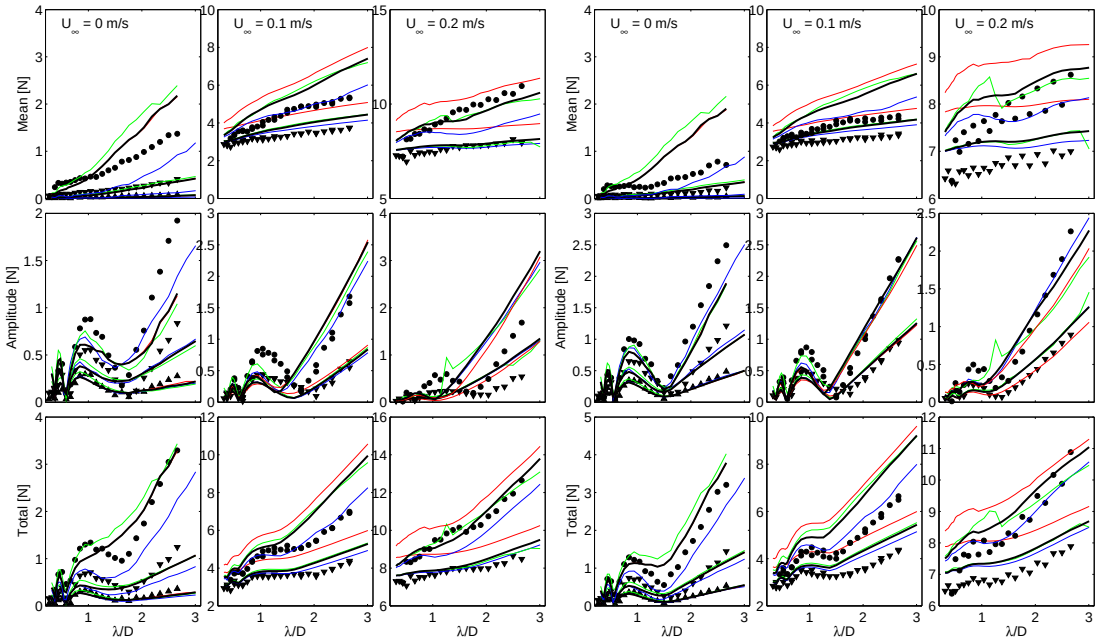

Figure 20: Numerical sensitivity study. Comparison of mean and total forces and force amplitudes in the front (left) and aft (right) mooring lines. Load parameters are varied, where numbers in brackets refer to parameter variation no. in Table 5. Blue: Wheeler stretching (1). Green: nonlinear Froude Kriloff and restoring forces (5). Red: flow reduction factor $r = 0$ (6).

Lader, P., H. Moe, Ø. Jensen, and E. Lien (2009). Nøter med høy soliditet - modellforsøk. Technical report, SINTEF Fisheries and Acquaculture (In Norwegian).

Lader, P. F. and A. Fredheim (2006). Dynamic properties of a flexible net sheet in waves and current - a numerical approach. *Aquacultural Eng. 35*, 228–238.

Li, P. and O. M. Faltinsen (2012). Wave-induced vertical response of an elastic circular collar of a floating fish farm. In *Int. Conf. on Hydrodynamics (ICHD), St. Petersburg, Russia*.

Li, P., O. M. Faltinsen, and A. Fredheim (2014). Wave-induced motions of a fish-farm elastic floater: Experimental and numerical studies. In *33rd Int. Conf. Ocean, Offshore and Arctic Engng. (OMAE2014-23302)*.

Løland, G. (1991). *Current Forces on and Flow through Fish Farms*. Ph. D. thesis, NTNU, Trondheim, Norway.

Marichal, D. (2003). Cod-end numerical study. In *3rd Int. Conf. on Hydroelasticity in Marine Technology, Oxford, UK*.

Moe, H., A. Fredheim, and O. S. Hopperstad (2010). Structural analysis of aquaculture net cages in current. *J. Fluids and Struct. 26*, 503–516.

Stansberg, C. T., O. T. Gudmestad, and S. K. Haver (2008). Kinematics under extreme waves. *J. Offshore Mech. Arctic Eng. 130*, 7.

Xu, T.-J., G.-H. Dong, Y.-P. Zhao, Y.-C. Li, and F.-K. Gui (2012). Numerical investigation of the hydrodynamic behaviors of multiple net cages in waves. *Aquacultural Engng. 48*, 6–18.

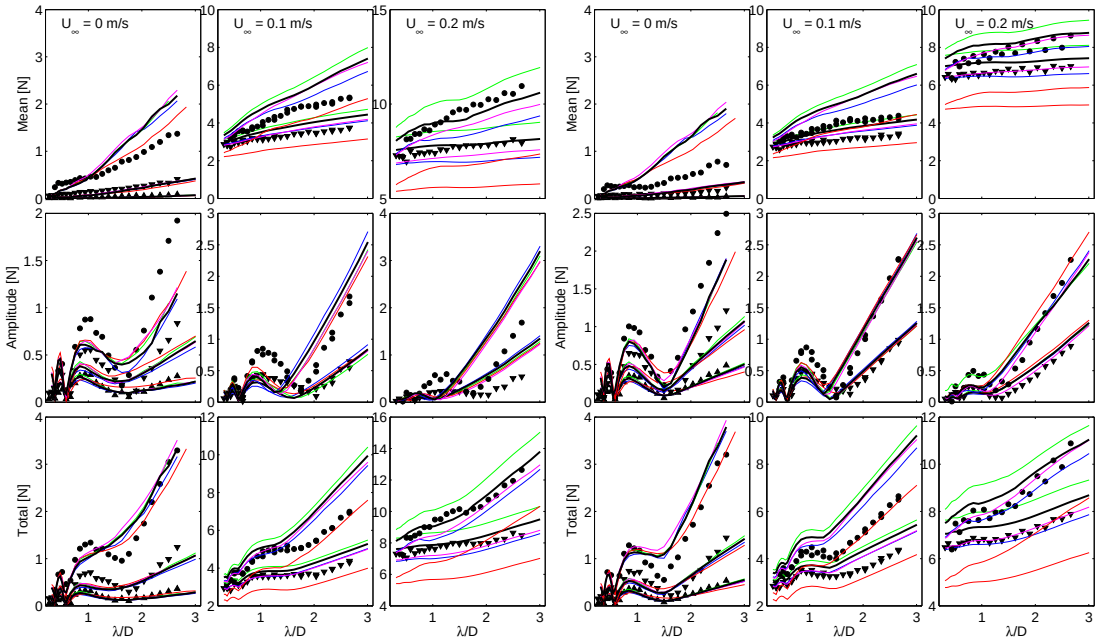

Figure 21: Same as Figure 20. Structural parameters varied. Blue: cross-sectional diameter $2c = 0.028$m (8). Green: $2c = 0.032$m (9). Red: $EI = 25EI_0$ (12). Purple: $T_{ax} = 10$N (14).

Zhao, Y. P., C. W. Bi, G. H. Dong, F. K. Gui, Y. Cui, and T. J. Xu (2013). Numerical simulation of the flow field inside and around gravity cages. aquacultural engineering. *Aquacultural Engng. 52*, 1–13.

Zhao, Y.-P., Y.-C. Li, G.-H. Dong, F.-K. Gui, and B. Teng (2007). A numerical study on dynamic properties of the gravity cage in combined wave-current flow. *Ocean Engng. 34*, 2350–2363.

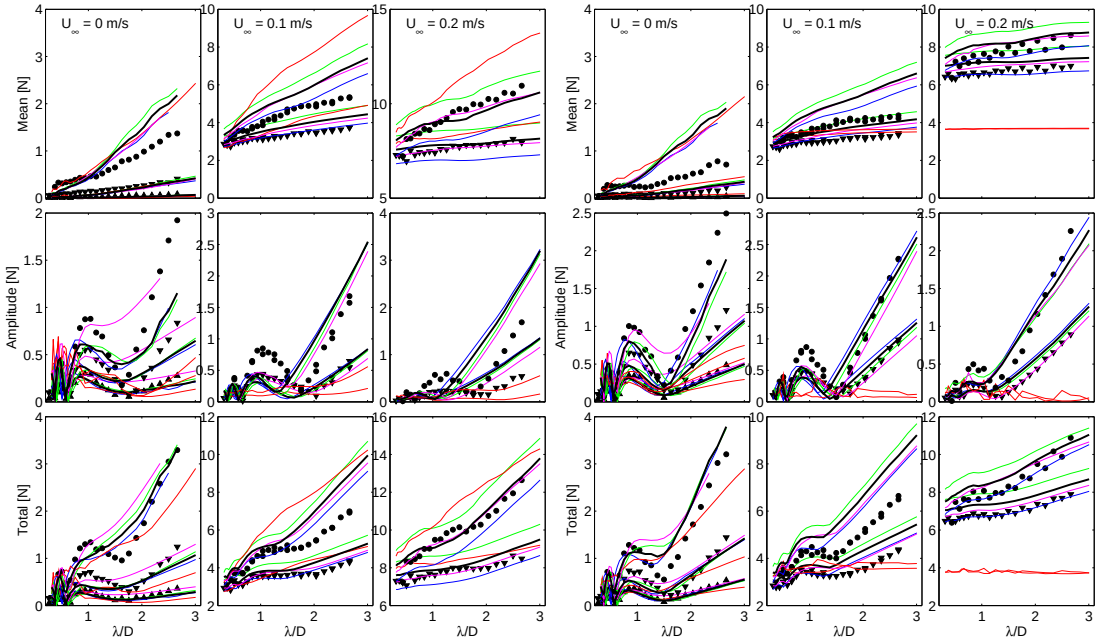

Figure 22: Same as Figure 20. Structural parameters varied. Blue: net and floater diameter $D = 1.35$m (17). Green: $D = 1.65$m (18). Red: $E_{\text{net}} = 1 \times 10^6 \text{Nm}^2$ (20). Purple: initial shape not vertical (23), see Figure 24.

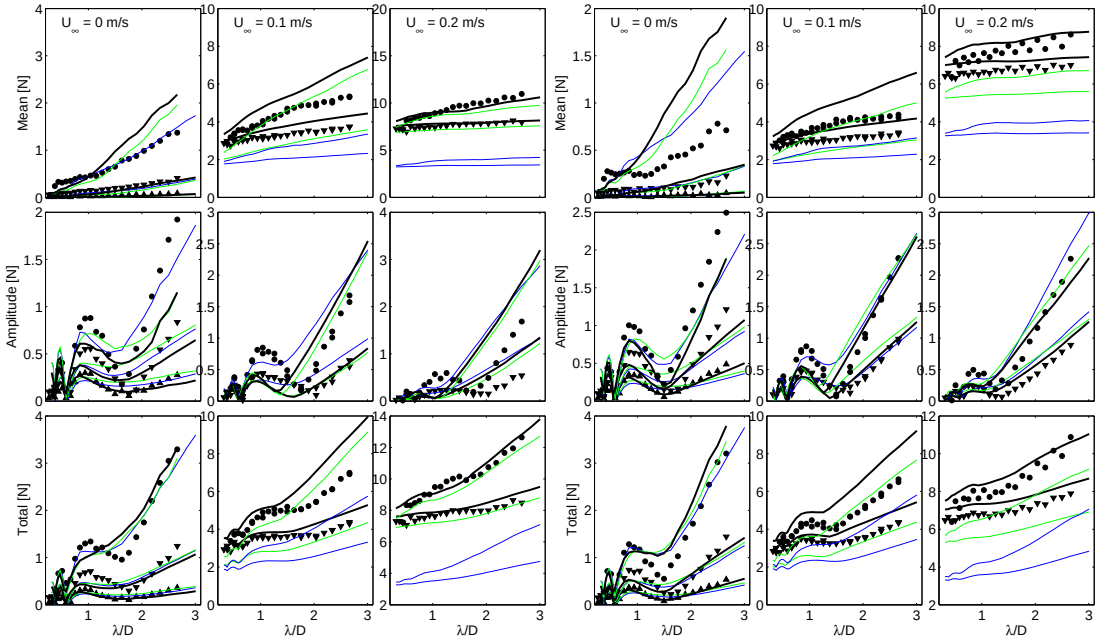

Figure 23: Same as Figure 20. Numerical parameters varied. Blue: no. of modes $N_h = 1$, $N_v = 2$ (29). Green: no. of modes $N_h = 4$, $N_v = 4$ (29).

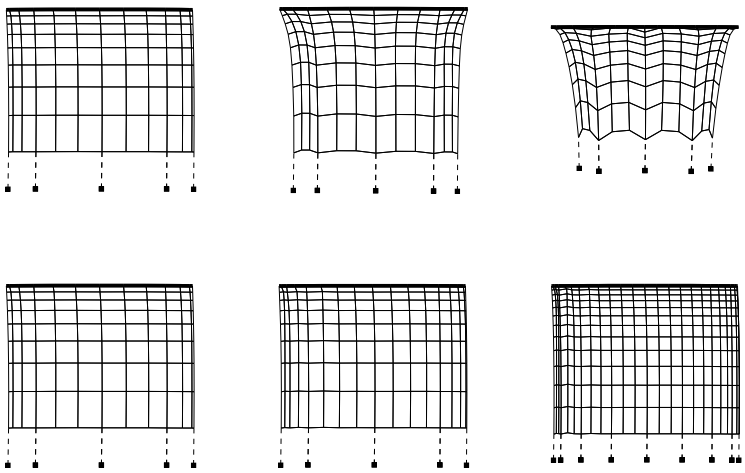

Figure 24: Examples of net shapes after first time-step of simulations. Upper row: Left: nominal net shape. Middle: the shape referred to as "Initial" net shape in the sensitivity study. Right: Elastic net. Lower row: net shapes with different resolutions. Left: nominal resolution, $N_H \times N_V = 24 \times 8$. Middle: $N_H \times N_V = 32 \times 8$. Right: $N_H \times N_V = 48 \times 12$. Note that the (appearent) long distance from the bottom of the net to the sinker weights is a consequence of the modelling of the net, as described in Kristiansen and Faltinsen (2012a).

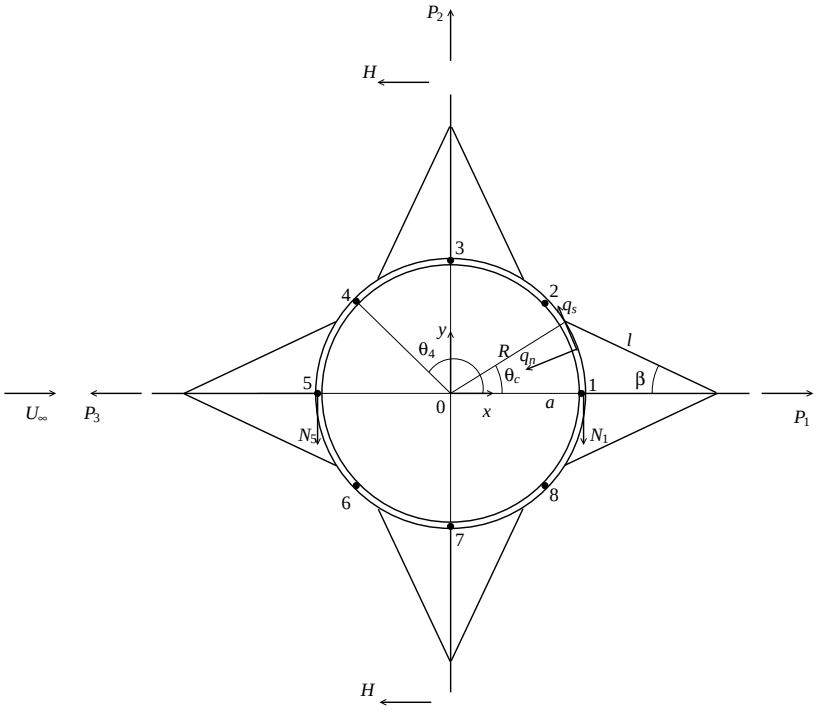

Figure 25: Illustration of simplified calculation method for obtaining approximate values of the axial tension T_{ax}. Note that P_2 is the $y-$component only of the line tension.

Appendix A

5.1 Axial tension in the floater - simplified calculations

The following is based on (Tore Søreide, personal communication 2012). The floater is divided in eight segments as illustrated in Figure 25. We assume that the axial tension T_{ax} is piecewise constant in each segment, denoted N_1 to N_5. Due to symmetry about the x-axis, N_6 to N_8 are not explicitly needed. $q_n(s)$ and $q_s(s)$ represents the normal and tangential forces from the net cage, parametrized by the arc length s around the floater. The viscous drag on the floater is not included in $q_n(s)$ and $q_s(s)$ in these calculations; they are small compared to the tensions due to the net cage.

We define the following geometrical relations:

$$
\begin{aligned}
l\sin\beta &= R\sin\theta_c && (21)\\
a &= l\cos\beta + R\cos\theta_c = R(\,\mathrm{atan}\,\beta\sin\theta_c + \cos\theta_c) && (22)\\
b &= a\tan\beta && (23)
\end{aligned}
$$

Global equilibrum of forces in the $x-$direction yields

$$P_1 = 2H + P_3 + 2\int_0^\pi (q_s(\theta)\sin\theta + q_n(\theta)\cos\theta)R\,\mathrm{d}\theta \qquad (24)$$

Global equilibrum of moments around the origin yields

$$N_1R - N_5R = Ha - \frac{P_1 - P_3}{2}b + \int_0^\pi (q_s(\theta)R\,\mathrm{d}\theta R \qquad (25)$$

Global equilibrum of forces in the $y-$direction yields

$$N_1 + N_5 = P_2 - \frac{P_1+P_3}{2}\tan\beta + \int_0^{\pi}(q_s(\theta)sin\theta - q_n(\theta)\cos\theta)R\,\mathrm{d}\theta \tag{26}$$

Combining the above equations and re-arranging terms gives the axial tensions as

$$\begin{aligned}
N_1 &= \frac{P_2}{2} - \frac{P_1+P_3}{4}\tan\beta + \frac{H}{2}(\ \mathrm{atan}\beta\sin\theta_c + \cos\theta_c) - \frac{P_1-P_3}{4}(\sin\theta_c + \tan\beta\cos\theta_c) \\
&+ \frac{1}{2}\int_0^{\pi}(q_s(\theta)(1+\cos\theta) - q_n(\theta)\sin\theta)R\,\mathrm{d}\theta \\
N_2 &= N_1\cos\theta_2 + \frac{P_1}{2\cos\beta}\sin(\theta_2+\beta) - \int_0^{\theta_2}(q_s(\theta)\cos(\theta_2-\theta) - q_n(\theta)\sin(\theta_2-\theta))R\,\mathrm{d}\theta \\
N_3 &= \frac{P_1}{2} - \frac{P_2}{2}\tan\beta - H - \int_0^{\pi/2}(q_s(\theta)\sin\theta + q_n(\theta)\cos\theta)R\,\mathrm{d}\theta \\
N_4 &= N_5\cos(\pi-\theta_4) + \frac{P_3}{2\cos\beta}\sin(\theta_4-\beta) + \int_{\theta_4}^{\pi}(q_s(\theta)\cos(\theta-\theta_4) - q_n(\theta)\sin(\theta-\theta_4))R\,\mathrm{d}\theta \\
N_5 &= P_2 - N_1 - \frac{P_1+P_3}{2}\tan\beta + \int_0^{\pi}(q_s(\theta)\cos\theta - q_n(\theta)\sin\theta)R\,\mathrm{d}\theta
\end{aligned}$$

The procedure we used in our numerical study is as follows. First, $N_1 - N_5$ are calculated in the zero-current case. That is, only pre-tension is applied. q_n and q_s are then zero if the net is hanging vertically. Next, a simulation with current is run until steady state, and $N_1 - N_5$ recalculated. These latter values are used throughout the simulation including both wave and current.

Relevant values of the axial stiffness for the present study as calculated by the above procedure are provided in Table 6.

Table 6: Values of axial stiffness $N_1 - N_5$ when a pre-tension of 14N is applied in all four mooring lines applied in the present study.

	$U_\infty = 0$m/s	$U_\infty = 0.1$m/s	$U_\infty = 0.2$m/s
N_1	5.66N	4.38N	3.14N
N_2	9.90N	9.83N	9.40N
N_3	5.66N	5.24N	4.80N
N_4	9.90N	9.24N	8.30N
N_5	5.66N	5.38N	5.51N